



Structural characterization of NrnC identifies unifying features of dinucleases

Justin D Lormand¹, Soo-Kyoung Kim², George A Walters-Marrah¹, Bryce A Brownfield³, J Christopher Fromme³, Wade C Winkler², Jonathan R Goodson², Vincent T Lee², Holger Sondermann^{1,4,5}*

¹Department of Molecular Medicine, Cornell University, Ithaca, United States; ²Department of Cell Biology and Molecular Genetics, University of Maryland, College Park, United States; ³Department of Molecular Biology and Genetics, Cornell University, Ithaca, United States; ⁴CSSB Centre for Structural Systems Biology, Deutsches Elektronen-Synchrotron DESY, Hamburg, Germany; ⁵Christian-Albrechts-Universität, Kiel, Germany

Abstract RNA degradation is fundamental for cellular homeostasis. The process is carried out by various classes of endolytic and exolytic enzymes that together degrade an RNA polymer to monoribonucleotides. Within the exoribonucleases, nano-RNases play a unique role as they act on the smallest breakdown products and hence catalyze the final steps in the process. We recently showed that oligoribonuclease (Orn) acts as a dedicated diribonuclease, defining the ultimate step in RNA degradation that is crucial for cellular fitness (Kim et al., 2019). Whether such a specific activity exists in organisms that lack Orn-type exoribonucleases remained unclear. Through quantitative structure-function analyses, we show here that NrnC-type RNases share this narrow substrate length preference with Orn. Although NrnC and Orn employ similar structural features that distinguish these two classes of dinucleases from other exonucleases, the key determinants for dinuclease activity are realized through distinct structural scaffolds. The structures, together with comparative genomic analyses of the phylogeny of DEDD-type exoribonucleases, indicate convergent evolution as the mechanism of how dinuclease activity emerged repeatedly in various organisms. The evolutionary pressure to maintain dinuclease activity further underlines the important role these analogous proteins play for cell growth.

*For correspondence: holger.sondermann@cssbhamburg.de

Competing interest: The authors declare that no competing interests exist.

Funding: See page 28
Received: 12 May 2021

Accepted: 08 September 2021
Published: 17 September 2021

Reviewing Editor: Bryce E Nickels, Rutgers University, United States

@ Copyright Lormand et al. This article is distributed under the terms of the Creative Commons Attribution License, which permits unrestricted use and redistribution provided that the original author and source are credited.

Introduction

Traditionally, nano-RNases – enzymes that act on short, typically 2–7 residue-long RNA substrates – have occupied a distinct role in RNA metabolism as they catalyze the final steps in RNA degradation. To date, three main enzyme families have been assigned this function (*Liao et al., 2018*): oligoribonucleases (Orn; *Cohen et al., 2015*; *Orr et al., 2015*; *Zhang et al., 1998*), nano-RNase A and B (NrnA and NrnB; *Fang et al., 2009*; *Mechold et al., 2007*), and nano-RNase C (NrnC; *Liu et al., 2012*). NrnA comprises DHH-DHHA1 domains and is suggested to act as a bidirectional exonuclease that cleaves short RNA fragments from 3' to 5' and longer substrates from 5' to 3' (*Mechold et al., 2007*; *Schmier et al., 2017*). Orn and NrnC are 3'–5' exonucleases with a DnaQ fold containing the catalytic DEDD motif (*Chin et al., 2006*; *Yuan et al., 2018*), a domain that is common in enzymes that act on nucleic acids. Notably, Orn (and its eukaryotic ortholog REXO2) or NrnC activity is critical for cellular growth, rendering them unique amongst the exoribonucleases known to date (*Ghosh and Deutscher, 1999*; *Liu et al., 2012*; *Nicholls et al., 2019*).

Despite its classification as a nano-RNase, we recently reported that Orn acts primarily as a diribonuclease, assigning it a highly specific and unique function in clearing the diribonucleotide pool as the



terminal step in RNA degradation. Substrate-bound structures of bacterial and human orthologs, Orn and REXO2, respectively, revealed the scissile bond of the dinucleotide surrounded by the conserved, catalytic DEDDh motif that is involved in divalent cation coordination and catalysis. More importantly, key determinants for the RNA length preference of Orn and REXO2 include a leucine residue that wedges between the two bases of the diribonucleotide and a phosphate cap – invariable residues that coordinate the 5'-phosphate on the substrate and limit substrate length to 2 nucleotides (*Kim et al.*, 2019). An independent study on REXO2 confirmed our structural analysis and established the human enzyme as a diribonuclease in mitochondria, where its activity alters gene expression (*Nicholls et al.*, 2019), a function that relates to the role of diribonucleotides in transcription initiation (*Druzhinin et al.*, 2015; *Goldman et al.*, 2011; *Nicholls et al.*, 2019; *Vvedenskaya et al.*, 2012).

Our previous work on Orn-type RNases was motivated by three main considerations: Orn's essential role for growth in many bacteria, its role in cyclic dinucleotide signaling, and a lack of understanding how substrate specificity towards short RNA substrates, and in turn lack of activity towards longer RNAs, is achieved (*Ghosh and Deutscher, 1999*; *Kamp et al., 2013*; *Kim et al., 2019*; *Orr et al., 2015*; *Palace et al., 2014*). The latter is a basic question as the unique substrate profile is the defining characteristic of this class of enzymes. We demonstrated that Orn has a much higher preference for diribonucleotides compared to 3–7 residue-long RNAs than anticipated previously. This selectivity is due to an active site that is exquisitely suited for diribonucleotides with a 5' phosphate. The enzyme's diribonuclease activity is required for normal bacterial growth and clearance of c-di-GMP breakdown products. Notably, a knock-out of *Pseudomonas aeruginosa* Orn can not only be complemented by various Orn orthologs, but also by the other three nano-RNases: NrnA, NrnB, and NrnC (*Orr et al., 2018*). However, it is not clear whether this functional complementary correlates with a narrow substrate specificity for dinucleotides.

A recent structural study of NrnC from the soil bacterium Agrobacterium tumefaciens identified a homo-octameric assembly as the enzyme's functional unit (Yuan et al., 2018). The unit can be divided into two stacked rings, each composed of four NrnC monomers, which together form a central channel lined with eight active sites. Mutagenesis of key active-site residues confirmed the requirement of the conserved DEDDy motif for catalysis and identified positively charged residues lining the channel, which are also important for function. Activity assays indicated single-stranded RNA and DNA as well as double-stranded DNA as potential substrates of NrnC; however, the structural basis for substrate specificity has not been established.

Here, we ask the fundamental question: What is the substrate specificity of NrnC-type enzymes, an RNase that is essential for the growth of Gram-negative bacteria such as Caulobacter crescentus, Bartonella henselae, and Brucella abortus (Christen et al., 2011; Liu et al., 2012; Sternon et al., 2018). We present crystal structures of NrnC from B. henselae and Brucella melitensis in their substrate-bound and apo states. The structures confirm an octameric assembly as a conserved feature of NrnC-type RNases. The substrate-bound states reveal, similar to Orn, a narrow active site that appears optimized for dinucleotides. This preference is reflected also in the enzyme's activity profile. A comparative genomics analysis indicates that Orn and NrnC, despite using a common DnaQ fold, evolved separately as isofunctional enzymes (Galperin and Koonin, 2012; Omelchenko et al., 2010). Considering also the distribution of the structurally unrelated, yet functionally overlapping NrnA- and NrnB-type RNases predominantly in organisms that lack Orn and NrnC underlines the importance to maintain diribonuclease activity for cellular function in the bacterial and eukaryotic domains of life.

Results and discussion

Overall structure of diribonucleotide-bound NrnC

The earlier observation that NrnC expression is able to complement a *P. aeruginosa orn* deletion strain indicates that both enzymes function on diribonucleotides (*Orr et al., 2018*), consistent with their initial classification as nano-RNases (*Datta and Niyogi, 1975*; *Liu et al., 2012*; *Niyogi and Datta, 1975*; *Yu and Deutscher, 1995*). However, while we showed that Orn acts as a dedicated diribonuclease (*Kim et al., 2019*), the structural basis for NrnC's substrate preference remained not well defined. Specifically, it was not clear how NrnC distinguishes between short RNAs and longer polymers. To answer this question, we determined crystal structures of wild-type *B. henselae* and *B. melitensis* NrnC (NrnC_{Bh} and NrnC_{Bm}, respectively) bound to pGG and, in the case of NrnC_{Bm}, also



in the substrate-free state. NrnC_{Bh} forms a homo-octameric assembly comprising two C4-symmetric rings (*Figure 1A*) as observed with the previously determined substrate-free, orthologous protein from A. tumefaciens (69% sequence identity compared to NrnC_{Bh}, monomer/octamer all-atom rmsd 0.4/1.3 Å; PDB:5ZO3; *Yuan et al.*, 2018). The two rings stack with the same face, tail-to-tail, forming a D4-symmetric octamer. The contacts between the subunits within each ring are dominated by a few polar interactions spanning between 441 and 512 Ų (*Figure 1—figure supplement 1A and B*; determined by PISA [*Krissinel and Henrick, 2007*]). In contrast, pairwise, homotypic interactions between the two rings involve an extensive hydrophobic interface of 1204 Ų via an antiparallel packing of the last helix of the NrnC fold. This mode of ring stacking positions the C-terminus of one monomer so that it reaches into the active site of the adjacent monomer in the other ring (*Figure 1—figure supplement 1A and C*).

The diribonucleotide pGG is bound to all eight active sites of the NrnC_{Bh} octameric assembly (*Figure 1B*). The active sites face the center of the central cavity formed by the NrnC octamer, positioned mid-way of each ring. In this crystallographic state, the residues of the catalytic DEDDy signature motif (D^{25} , E^{27} , D^{84} , D^{155} , Y^{151}) are primed for accepting divalent metal ions for nucleotide hydrolysis. The side chain of Y^{151} coordinates a water molecule, which likely serves as the attacking nucleophile in the reaction (*Figure 1C*).

The structure also reveals the molecular basis for substrate coordination. Reminiscent of Orn's active site, the bases of the diribonucleotide are splayed apart by a leucine residue, or L-wedge (L³¹) (*Figure 1C*). Continuing with the parallels to Orn, the 5' phosphate of pGG is coordinated by several residues forming a 'phosphate cap,' in this case basic residues H⁷⁹, K¹⁰³, and H²⁰⁵, the latter being the second to last residue of the protein, contributed from a subunit from the adjacent ring. The specific motifs coordinating the substrate are invariable in NrnC orthologs, in contrast to the exterior surface with overall lower conservation (*Figure 1D*), and culminate in a length-restricted active site that appears optimized for diribonucleotides. A comparison with the structurally related Rrp6 exonuclease subunit of the exosome bound to a longer RNA substrate supports this notion as residues K¹⁰³ and H²⁰⁵ of NrnC's phosphate cap directly block the path for longer substrates (*Figure 1—figure supplement 2A and C*; *Wasmuth et al., 2014*). Similarly, RNase D, a homologous exoribonuclease that processes longer and stable RNA molecules, presents a more expansive, open active site, although the lack of a substrate-bound structure prevents a more direct comparison of this state (*Figure 1—figure supplement 2B and C*; *Zuo et al., 2005*).

Similar binding poses to pGG at NrnC were observed with pAA and pGC (*Figure 1—figure supplement 3A–C*), suggesting that most if not all diribonucleotides can be accommodated by NrnC. A co-crystal structure with the di-phosphorylated mononucleotide pAp, a metabolite described as an inhibitor of NrnC (*Liu et al., 2012*), shows the ligand predominantly occupying the 5' position of the active site with the 3' phosphate engaging the catalytic motif and the 5' phosphate being coordinated by the phosphate cap of NrnC (*Figure 1—figure supplement 3D*).

To establish the functional relevance of the crystallized state of NrnC, we initiated *in crystallo* catalysis by soaking NrnC_{Bh}•pGG co-crystals in solutions with divalent cations, magnesium (Mg²⁺) or manganese (Mn²⁺). The enzyme became catalytically active with the addition of either cation, with the resulting electron densities showing a broken phosphodiester bond (*Figure 1—figure supplement 4*). The experiments also confirmed a two-metal mechanism first by interpretation of electron density upon Mg²⁺ soaking (*Figure 1—figure supplement 4A*). The placement of active site metal atoms was subsequently confirmed using anomalous data collected on Mn²⁺-soaked crystals (see anomalous difference map, *Figure 1—figure supplement 4B*). In these post-catalysis structures, the 5' GMP appears to leave the active site first, as suggested by weaker electron density indicative of lower mononucleotide occupancy at the 5' site compared to the 3' site.

The characteristic active-site motifs of NrnC_{Bh} contribute to diribonuclease activity

The structural analysis revealed the molecular basis for substrate binding to NrnC, identifying molecular features that constrain the active site. To assess their relevance for NrnC's catalytic activity, we tested tag-less, purified NrnC_{Bh} and structure-based point mutants thereof in an in vitro activity assay. All mutant proteins retained their quaternary structure and purified as octamers, indistinguishable from wild-type NrnC (*Figure 2—figure supplement 1*). 5'- 32 P-radiolabeled pGG was incubated with



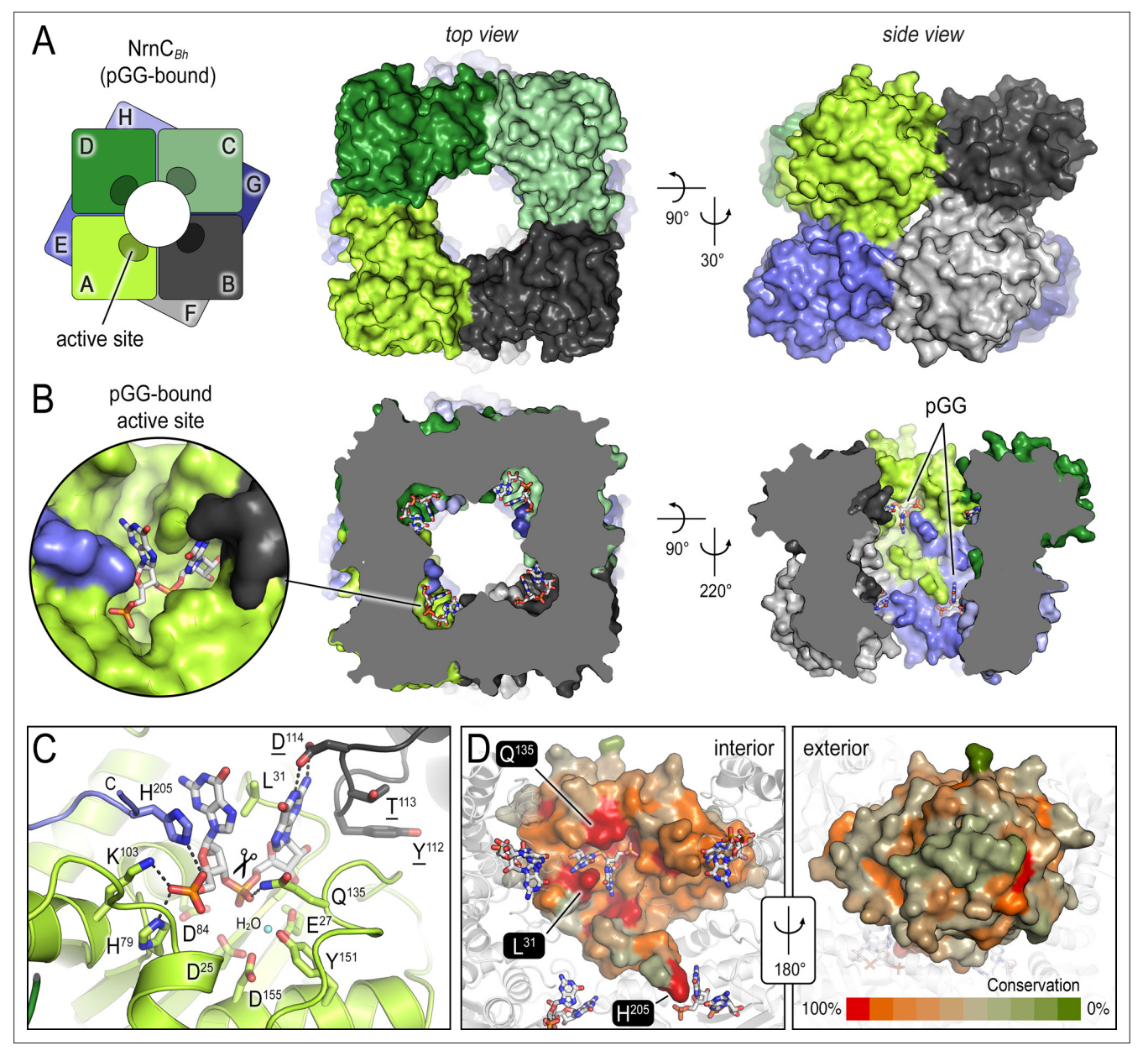


Figure 1. The crystal structures of *B. henselae* nano-RNase C (NrnC) bound to pGG reveals motifs defining substrate specificity. (**A**) The octameric assembly. NrnC_{Bh} is shown as surface representation in two views. Each monomer is shown in a distinct color. The cartoon illustrates the stacking of the two tetrameric NrnC rings that form the octamer with a central, round opening. (**B**) Active-site position. Each monomer contributes one active site, here bound to the substrate pGG, facing toward NrnC's central pore. Each active site includes a C-terminal tail of a subunit from an adjacent ring. (**C**) Substrate coordination. The catalytic DEDDy motif and residues coordinating each moiety of pGG contacts are shown as sticks, with carbon residues colored according to monomer identity. Residue Y¹⁵¹ coordinates water molecule near the scissile bond. (**D**) Conservation mapping on a surface representation of a NrnC monomer. Conservation scores were calculated based on a multisequence alignments (MUSCLE; **Edgar, 2004**) of NrnC homologs identified using a sequence search on the EggNOG resource, version 5.0.0 (**Huerta-Cepas et al., 2019**) and the sequence of NrnC_{Bh} as the input. Outliers were identified based on sequence length and non-consensus insertions, resulting in a final collection of 560 sequences of putative NrnC orthologs. The two views, separated by a 180° rotation, show the cavity-facing (interior, left) and outer-facing (exterior, right) surface regions.

The online version of this article includes the following figure supplement(s) for figure 1:

Figure supplement 1. Inter- and intra-ring contacts in the $NrnC_{Bh}$ octamer.

Figure supplement 2. Comparison of nano-RNase C (NrnC) to structurally related proteins reveals the constricted nature of NrnC's active site.

Figure supplement 3. Structural comparison of $NrnC_{Bh}$ bound to various ribonucleotides.

Figure supplement 4. In crystallo catalysis indicates a two-metal mechanism of NrnC_{Bh} activity.



wild-type or mutant enzymes in the presence of divalent cations at physiological ionic strength. Quenched reactions were resolved via urea-denaturing PAGE to observe nucleolytic cleavage over time (*Figure 2A*). With wild-type NrnC_{Bh}, the majority of pGG was processed already by the first time point at 30 s, and complete cleavage of pGG to GMP was achieved by 3 min. Nucleolytic activity on pGG was completely inhibited by alanine mutation of the catalytic DEDDy motif residues D²⁵ and Y¹⁵¹. Intermediate cleavage kinetics were evident with proteins with disrupted leucine wedge (NrnC_{Bh}-L³¹A) as well as the phosphate cap (NrnC_{Bh}-H⁷⁹A, -K¹⁰³A, or -H²⁰⁵A). NrnC binding to and activity on pGG were slightly inhibited by pAp (*Figure 2B and C*). In contrast, the diguanylate compound GG, which lacks a 5' phosphate, did not inhibit NrnC's binding to or activity on pGG (*Figure 2B and C*), further elaborating on the importance of the interaction between phosphate cap residues and the 5' phosphate for NrnC function.

We previously proposed a model of cellular fitness in which the loss of *orn* leads to toxic diribonucleotide accumulation that is detrimental to the cell. The *orn* deletion in *P. aeruginosa* manifests as small-colony growth, which is reversible by complementation with *orn* or other nano-RNases expressed from a plasmid (*Figure 2D*; *Kim et al., 2019*; *Orr et al., 2018*). Here we used the rescue of the small colony phenotype as a readout of NrnC diribonuclease activity in cells, quantified as colony size. Complementation of the deletion strain with wild-type NrnC_{Bh} (with a C-terminal HA tag for detection) restored normal colony size, while NrnC alleles containing mutations within the DEDDy motif failed to complement (*Figure 2D*). Further, NrnC alleles containing mutations in the L-wedge or the phosphate cap showed reduced complementation effects (L³¹A, K¹⁰³A, K¹³²A, or H²⁰⁵A; *Figure 2D*). NrnC_{Bh}-H⁷⁹A failed to complement the *orn* deletion. Western blot analysis established protein expression for all mutant and wild-type NrnC variants, with the exception of NrnC_{Bh}-H⁷⁹A, which expressed poorly in *P. aeruginosa*, preventing a distinction between failure to rescue because of the mutation or protein levels, or both (*Figure 2—figure supplement 2*). Together, these data confirm the importance of the motifs identified in the substrate-bound NrnC structures for the enzyme's diribonuclease activity in vitro and in cells.

Structural comparison of NrnC substrate-bound states reveals an active site optimized for dinucleotides

To further understand the structural basis of NrnC's substrate preference, we determined structures of *B. melitensis* NrnC (NrnC_{Bm}) in several apo and partially pGG-bound states. The overall structure of pGG-bound NrnC_{Bm} is virtually identical to NrnC_{Bh}, namely a homo-octameric assembly with eight active sites pointing toward the central channel (*Figure 3A and B*). The acidic active site residues (D²⁴, E²⁶, D⁸³, D¹⁵⁴, and Y¹⁵⁰) as well as the L-wedge (L³⁰) and phosphate cap (H⁷⁸, K¹⁰², and H²⁰⁴) are structurally and functionally conserved.

NrnC_{8m} incubated with pGG crystallized with two molecules per asymmetric unit, only one of which was bound to the dinucleotide. The resulting octameric assembly contains alternating apo- and pGGbound subunits per tetrameric ring (Figure 3B). This mixed-state structure allowed us to propose features modulating substrate binding. In substrate-bound monomers (including in the structures of NrnC_{8b}), the DEDDy residue Y¹⁵⁰ points inward toward the scissile phosphodiester bond, coordinating the attacking water. In contrast, the Y150 side chain points away from the active site in substratefree NrnC (Figure 3A and B). A loop from an adjacent subunit that mediates inter-ring contacts between the monomers and that includes residue D113 buttresses the 3' base of the substrate. While the octameric assembly remains in the absence of substrate, this loop moves outward from the active site and D¹¹³ rotates away from the substrate (*Figure 3D*). The most drastic conformational change however is attributed to a flexible loop spanning residues 130SKQQQS135. This loop is ordered and positioned in contact with the dinucleotide in both ortholog structures (Figures 1C and 3B and C). In this state, residue Q^{134} of $NrnC_{Bm}$ (or Q^{135} in $NrnC_{Bh}$) contacts the scissile phosphate via a hydrogen bond; K¹³¹ (or K¹³² in NrnC_{8h}) points toward the 5' phosphate, thus contributing to the phosphate cap. In contrast, in the substrate-free state $NrnC_{Bm}$, captured in the mixed-state structure or a homogeneous apo-state structure, this loop swings away from the active site or is completely disordered, leading to an overall widening of the active site (Figure 3A; Figure 1—figure supplement 2C).

In a second apo-NrnC_{Bm} crystal form, we captured an alternate conformation in which the conserved hydrophobic residue F^{79} moves into the active site (*Figure 3—figure supplement 1*). The movement of this residue, which is adjacent to the phosphate cap residue H^{78} , is realized through a flip of the



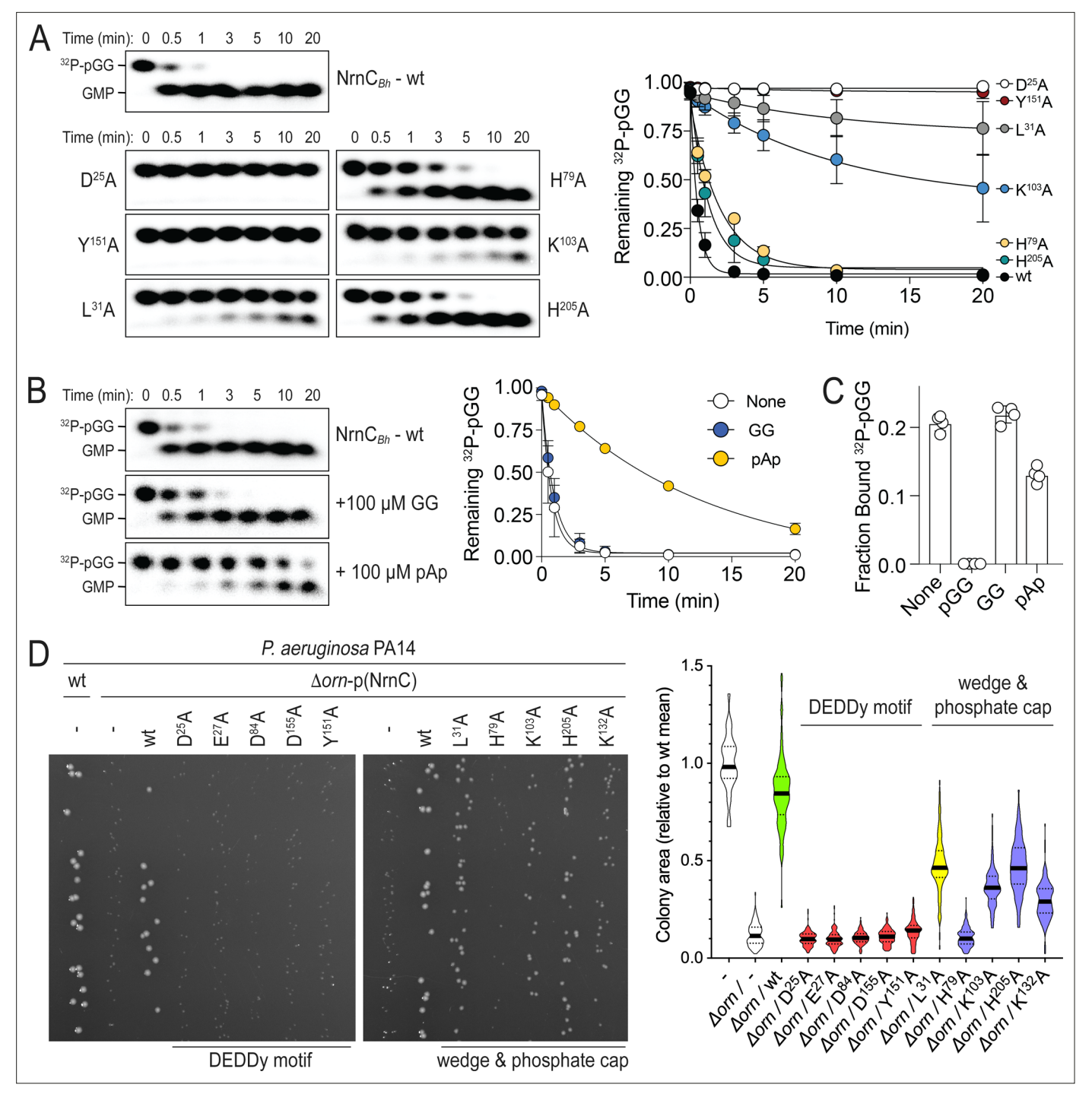


Figure 2. Phosphate cap and L-wedge contribute to nano-RNase C's (NrnC's) diribonuclease activity. (**A**) In vitro enzyme activity. Degradation of ³²P-pGG (1 μM total) by purified wild-type NrnC_{Bh} or variants with alanine substitutions (5 nM) at the indicated sites was assessed. Samples were stopped at the indicated times (min) and analyzed by denaturing 20% PAGE. Representative gels are shown (left). The graph (right) shows the means and SD of three independent experiments. (**B**) Effect of a dinucleotide lacking the 5′ phosphate (GG) and pAp on NrnC catalysis. pGG processing was assessed as in (**A**) but in the presence or absence of 100-fold excess (over ³²P-pGG) GpG or pAp. Representative gels (left) and quantification from three independent experiments (right) are shown. Means and SD are plotted. (**C**) Competition binding studies. Fraction bound of ³²P-pGpG to 200 nM purified NrnC_{Bh} in the presence of no competitor, 100 μM pGG, 100 μM GpG, or 100 μM pAp is plotted as individual data, means, and SD of four independent experiments. (**D**) Complementation of the small-colony phenotype of *P. aeruginosa* Δ*orn* by wild-type and mutant NrnC_{Bh}. Bacterial cultures were diluted and dripped on LB agar plates. After overnight incubation, representative images of the plates were taken (left). Experiments were performed in triplicate. Quantification of respective colony sizes is shown as violin plots (right).

Figure 2 continued on next page



Figure 2 continued

The online version of this article includes the following figure supplement(s) for figure 2:

Source data 1. Source data for Figure 2A.

Source data 2. Source data for Figure 2B.

Source data 3. Source data for Figure 2C.

Source data 4. Source data for Figure 2D.

Figure supplement 1. SEC-MALS of $NrnC_{Bh}$ wild-type and mutant variants.

Figure supplement 2. Expression of NrnC_{Bh} wild-type and mutant variants in P. aeruginosa Δ orn.

Figure supplement 2—source data 1. Original and labeled, unedited western blot image.

peptide backbone and would introduce a clash with the nucleotide. In the same structure, the flexible SKQQQS loop is collapsed into the active site, trapping the catalytic residue Y¹⁵⁰ in an intermediate conformation, which would introduce further clashes with the nucleotide substrate. Simultaneously, a rotamer change of the phosphate-cap residue H²⁰⁴ pivots its sidechain away from the active site, opening it for access to substrates (*Figure 3—figure supplement 1*). This conformation may depict a post-hydrolysis state, suggesting a mechanism for product release.

Analysis by cryo-electron microscopy supports a narrow substrate preference of NrnC in solution

Efforts to crystallize NrnC bound to longer substrates yielded structures with either empty active sites or with only pGG being resolved in the resulting electron densities. Residual RNase activity over the course of the crystallization or an impact of the longer substrates on crystal packing could contribute to the inability to resolve longer substrates, assuming they bind in the first place. As an alternative to crystallography, we determined $NrnC_{Bh}$ structures bound to pGG, pAGG, and pAAAGG by cryo-electron microscopy (cryo-EM), a technique that can visualize complexes formed after short equilibration periods and does not rely on proteins packing in a lattice. Considering that NrnC forms an octamer as the biological unit, we processed each data set with C1 and D4 symmetry, with the resulting models consisting of eight independent or an averaged chain, respectively (resolutions range from 2.72 to 3.27 Å; Figure 4, Figure 4—figure supplements 1-8). Processing with C1 symmetry preserves the individuality of each monomer allowing the observation of differences, for example, between active sites within the octamer. Applying D4 symmetry during processing averages all eight monomers, yielding a consensus model; however, regions with conformational differences between individual monomers may contribute to apparent disorder in the electron density maps. In an additional experiment with the 5-mer pAAAGG as the substrate, CaCl₂ was added to the buffer to probe whether the addition of Ca²⁺ ions, which prevent catalysis but can support substrate binding, has an effect on the binding of longer RNAs.

The structure of pGG-bound $NrnC_{Bh}$ confirmed all active site features described above based on the crystallographic data, namely a narrow active site, a phosphate cap coordinating the 5' phosphate of the substrate, a L-wedge splaying apart the two bases, and an active-site facing, well-resolved SKQQQS loop (*Figure 4A*, *Figure 4—figure supplement 9A*). Refinement with lower and higher symmetry resulted in comparable density maps, indicating a consensus state with eight nearly identical active sites.

The density maps of NrnC bound to any of the longer substrates resolved invariably only a diribonucleotide at the active site (with poorer density indicating the position of the ribose of the third nucleotide from the 3' end) (*Figure 4B*). The remainder of the longer substrates appeared disordered. Using D4-symmetry-averaged data, we also noticed consistently disorder of the SKQQQS loop (*Figure 4B*). Inspection of symmetry-less (C1) density maps revealed different loop conformations in the individual monomers of the octamers that, when symmetry-averaged, result in the apparent disorder (*Figure 4—figure supplements 5–8*). Notably, the majority of monomers contain a disengaged loop conformation, leaning away from the active site. Addition of Ca²⁺ with the pAAAGG substrate results in increased ordering of the loop in a disengaged state, similar to that observed in the substrate-free crystal structures of NrnC_{Bm} (*Figure 3E*, *Figure 4—figure supplement 9B*). Together, these results suggest that longer substrates may bind NrnC, but only the first two 3' nucleotides are



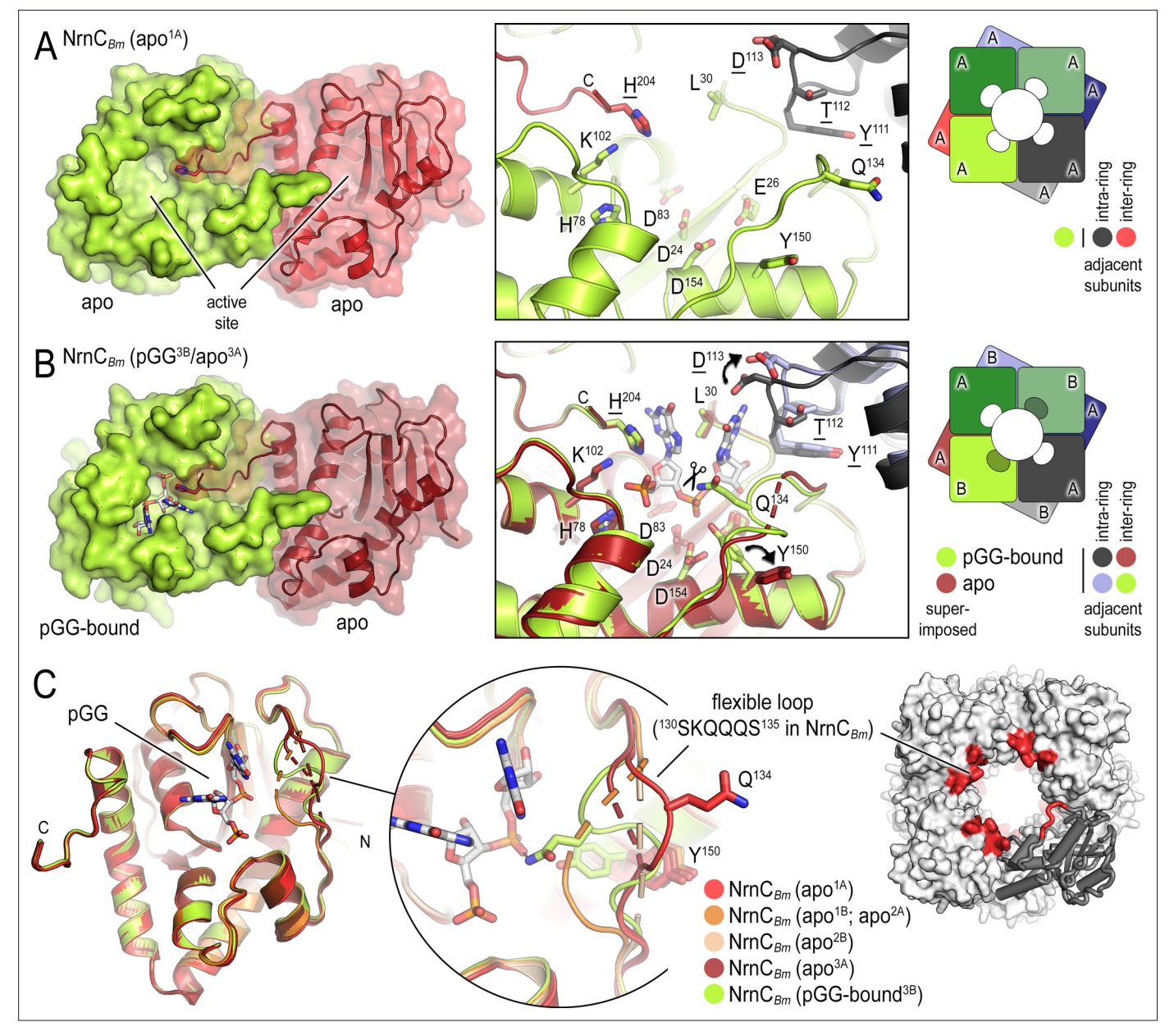


Figure 3. *B. melitensis* nano-RNase C (NrnC) crystal structures reveal a flexible loop that constraints the enzyme's active site. (**A**) Crystal structure of apo-NrnC_{Bm}. A crystallographic dimer as part of the octameric assembly is shown as surface presentation (left) and close-up of the active site (middle). The diagram (right) depicts the octamer and the spatial relationship of the monomers shown. (**B**) Crystal structure of NrnC_{Bm} with alternating substrate-bound and empty active sites. The close-up (middle) shows a superposition of the two monomers in the asymmetric unit, depicting their conformational difference and adjacent monomers, with intra- and inter-ring neighbors colored as shown in the diagram (right). (**C**) Superposition of four apo-NrnC_{Bm} conformations based on three independent crystal forms (comprising chains apo^{1A}/apo^{1B} for form 1; apo^{2A}/apo^{2B} for form 2, and apo^{3A}/pGG-bound^{3B} for form 3), compared to the pGG-bound conformation of the same protein shown in (**B**). The position of the flexible loop (red) in the NrnC octamer is shown (right panel).

The online version of this article includes the following figure supplement(s) for figure 3:

Figure supplement 1. Overlay of an alternative crystallographic apo-NrnC_{Bm} state with the apo- and pGG-bound states observed in the crystal structure shown in *Figure 3B*.

well coordinated at the active site. Furthermore, RNAs with more than two residues in length increase conformational variability at the active site, likely impacting catalytic activity toward those substrates. The SKQQQS loop may act as an activation loop that needs to swing into the active site, adopting a distinct, ordered conformation. The conformational change, induced by dinucleotide binding,



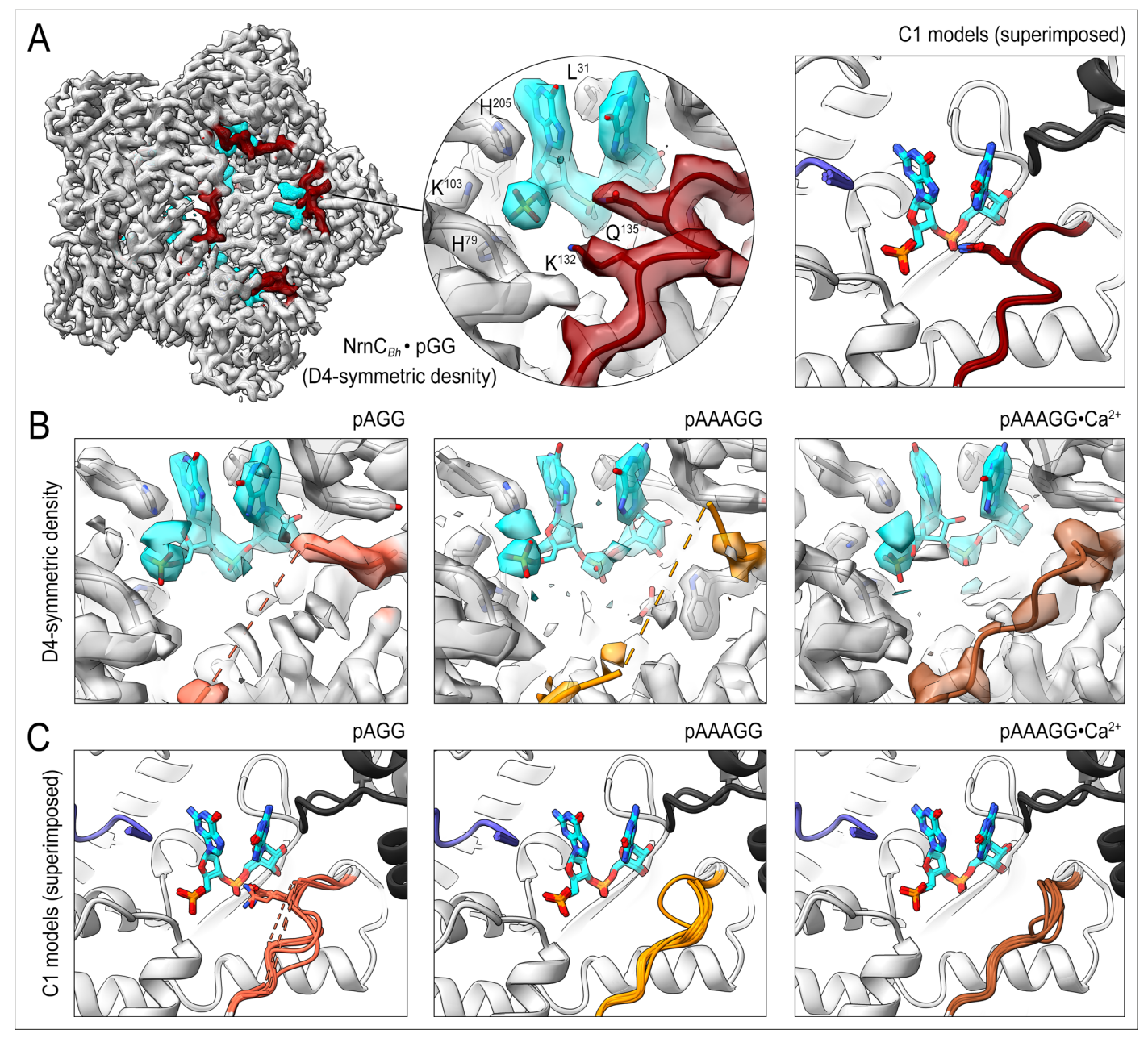


Figure 4. Cryo-electron microscopy (cryo-EM) structures of NrnC_{Bh} with 2-, 3-, 5-mer RNA substrates show substrate length-dependent active site conformations. (**A**) Electron density map of a NrnC_{Bh} octamer in complex with pGG. D4 symmetry was applied during final map refinement. pGG molecule and density are colored cyan. The SKQQQS-containing loops (residues 130–137) are colored maroon. Superposition of all eight active sites from a reconstruction with C1 symmetry (right panel) shows consensus order in the loop when bound to pGG. (**B**) Active site images shown for NrnC_{Bh} incubated with 3-mer and 5-mer (with or without Ca²⁺) RNA substrates. Regions corresponding to those shown in (**A**) are shown in color, with light red (left panel), orange (middle panel), and brown (right panel) depicting the loop/loop density from structures determined with added pAGG, pAAAGG, and pAAAGG•Ca²⁺, respectively. D4-symmetric maps are shown. (**C**) Superposition of all eight active sites from octamer reconstructions based on respective C1-symmetric maps for each RNA substrate. Color scheme is as described in (**B**).

The online version of this article includes the following figure supplement(s) for figure 4:

Figure supplement 1. Cryo-electron microscopy (cryo-EM) workflow and resolution for $NrnC_{Bh} \circ pGG$.

Figure supplement 2. Cryo-electron microscopy (cryo-EM) workflow and resolution for NrnC_{Bh}•pAGG.

Figure supplement 3. Cryo-electron microscopy (cryo-EM) workflow and resolution for NrnC_{Bh}•pAAAGG.

Figure supplement 4. Cryo-electron microscopy (cryo-EM) workflow and resolution for NrnC_{Bh}•pAAAGG in the presence of Ca²⁺ ions.

Figure supplement 5. Overall and individual active site electron density of a NrnC_{Bh}•pGG octamer after refinement with C1 symmetry.

Figure 4 continued on next page



Figure 4 continued

Figure supplement 6. Overall and individual active site electron density of a NrnC_{Bh}•pAGG octamer after refinement with C1 symmetry.

Figure supplement 7. Overall and individual active site electron density of a NrnC_{8h}*pAAAGG octamer after refinement with C1 symmetry.

Figure supplement 8. Overall and individual active site electron density of a $NrnC_{Bh} \bullet pAAAGG$ octamer in the presence of Ca^{2+} ions after refinement with C1 symmetry.

Figure supplement 9. The conformation of nano-RNase C (NrnC) bound to substrates with more than two bases resembles the crystallographic apostate

correlates with the positioning of the catalytic tyrosine residue of the DEDDy motif in a catalytically competent position (also illustrated in *Figure 3—figure supplement 1*). Likewise, the SKQQQS loop would have to move out of the way to allow for substrate binding. In summary, the combined structural data indicate NrnC is optimized for dinucleotide processing over longer substrates, mirroring our analysis of Orn and REXO2 (*Kim et al., 2019*; *Nicholls et al., 2019*).

NrnC_{Bh} acts preferentially on dinucleotides

Although the structural analysis revealed a narrow active site akin to that of Orn, NrnC's substrate length preference has not been assessed formally in this new context. To address this, we conducted kinetic experiments with RNAs of increasing length as substrates, following protocols established for Orn (Kim et al., 2019). In the initial assay, RNAs with two or more residues were in 200-fold abundance over NrnC, a condition where NrnC turned over the entire pGG pool within 1 min (Figure 5A). In comparison to NrnC's expedient activity on pGG, increasing the substrate length by only a single residue (pAGG) resulted in a striking decrease of nucleolytic cleavage under otherwise identical conditions. For RNAs with four and more residues, the substrate was processed incompletely and a band indicative of a cleavage product that was one base shorter at the 3' end slowly increased over the course of the experiment (Figure 5A and B). Increasing the concentration of NrnC increased activity on the longest substrate tested, an RNA with seven bases (5'-32P-labeled AAAAAGG, pAAAAAGG), but full conversion to mononucleotides required a ratio of 1:1 NrnC:RNA, indicating a comparatively inefficient, and likely less physiological mechanism (Figure 5B). Furthermore, and similar to the kinetics observed with Orn (Kim et al., 2019), a diribonucleotide intermediate was undetectable with enzyme concentrations that were required to observe the successive breakdown of the longer RNA, revealing the rapid turnover of dinucleotides, proceeding at much faster timescales than with any other intermediate that could be readily observed (Figure 5B).

Quantification of NrnC's binding to radiolabeled RNA substrates of different length agreed with the preference of NrnC to cleave diribonucleotides. Affinities of NrnC for radiolabeled substrates (2–7-mer RNA) were determined at physiological ionic strength and in the presence of Ca^{2+} to inhibit any potential residual catalysis (*Rosta et al., 2014*). NrnC_{Bh} bound to pGG with a K_d = 17.7 nM. Increasing substrate length by just one additional residue resulted in a nearly 200-fold decrease in affinity (K_d pAGG = 3.49 µM; *Figure 5C*). RNA substrates of four, five, or six residues showed similar decreases in affinity, while a 7-mer RNA substrate showed intermediate binding strength with a 32-fold decrease from pGG (K_d pAAAAAGG = 576 nM). As another method to assess substrate preference, competition experiments were performed by incubating NrnC_{Bh} with 32 P-pGG with or without unlabeled RNAs of different length. While unlabeled pGG was able to displace radiolabeled pGG quantitatively on NrnC, longer substrates were less potent competitors under otherwise identical conditions (*Figure 5—figure supplement 1*). Together, the combined structural and biochemical results argue for a strong preference of NrnC toward the shortest species of RNAs, diribonucleotides with a 5' phosphate.

NrnC_{Bh} processes DNA under specific experimental conditions

The A. tumefaciens NrnC octamer was previously interpreted as a conduit for long, polymeric substrates, in particular single-stranded RNA and single-stranded or double-stranded DNA (dsDNA), based on the octamer's channel dimensions and positioning of the active sites (**Yuan et al., 2018**). DNase activity was proposed to allow NrnC octamers to act on opposite ends of dsDNA to completely unwind and degrade it by passing the strand through the central channel. Here, we asked whether NrnC_{Bh} could act on DNA substrates (**Figure 5—figure supplement 2**). Under near-physiological ionic



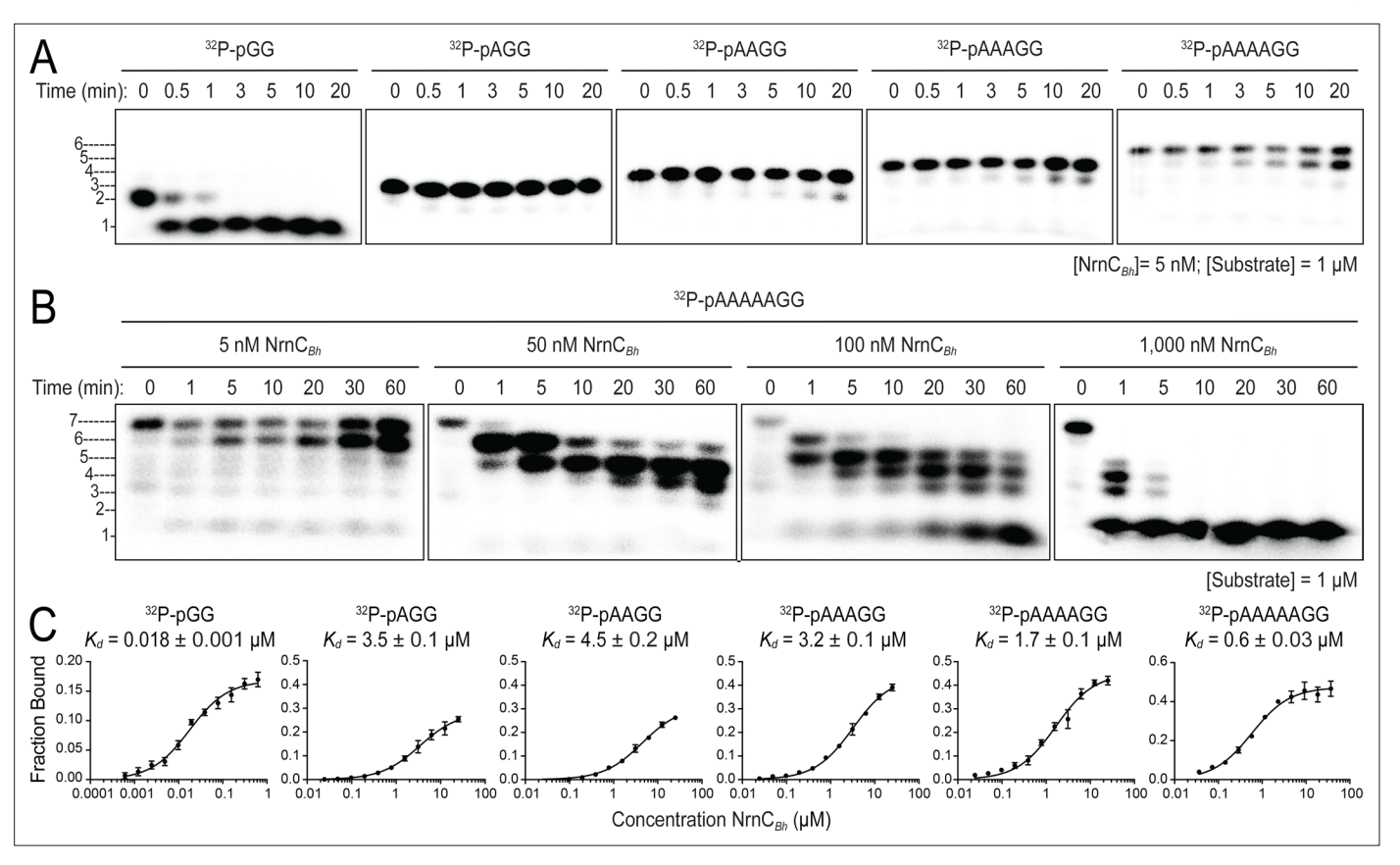


Figure 5. Nano-RNase C (NrnC) shows a strong preference for substrates with two residues in length. (**A**, **B**). RNase assays. Experiments are similar to those in *Figure 2* but were performed with radiolabeled substrates from 2 to 7 residues in length. Representative gels of at least two independent experiments are shown. In (**B**), enzyme concentration was varied from 5 to 1000 nM (1:200 to 1:1 enzyme:substrate ratio). Substrate length-dependent binding studies. (**C**) Affinity of NrnC for RNA with different lengths. Fraction bound of radiolabeled substrates of increasing length was assessed at different NrnC concentrations and is plotted as means and SD from three independent experiments.

The online version of this article includes the following figure supplement(s) for figure 5:

Source data 1. Source data for Figure 5A.

Source data 2. Source data for Figure 5B.

Source data 3. Source data for Figure 5C.

Figure supplement 1. Competition binding studies.

Figure supplement 1—source data 1. Quantification of ³²P-pGG binding to nano-RNase C (NrnC) in the presence of unlabeled RNA with increasing length (in three replicates).

Figure supplement 2. NrnC_{Bh} degrades long DNA fragments under distinct conditions.

Figure supplement 2—source data 1. Original, unedited agarose gel images and composite overview of nano-RNase C (NrnC) activity against 1.5 kb, double-stranded DNA substrates.

Figure supplement 3. The preferred substrates of $NrnC_{Bh}$ are diribonucleotides and deoxy-dinucleotides.

Figure supplement 3—source data 1. Source data for Figure 5—figure supplement 3B.

Figure supplement 3—source data 2. Source data for Figure 5—figure supplement 3C.

Figure supplement 3—source data 3. Source data for Figure 5—figure supplement 3D and E.

strength and in the presence of either Mg^{2+} or Mn^{2+} ions, $NrnC_{Bh}$ failed to degrade a 1.5-kb-long dsDNA fragment (*Figure 5—figure supplement 2B and C*). Degradation of dsDNA was only observed at low ionic strength (~0–60 mM NaCl) and only in the presence of Mn^{2+} ions, conditions that match those used for *A. tumefaciens* NrnC. The requirement for Mn^{2+} for activity on DNA substrates mirrors the previously reported phenomenon observed with the 3'–5' exonuclease EXD2 that acts on both ribo- and deoxyribonucleotides (*Park et al., 2019*).



To examine whether potential NrnC activity on dsDNA was dependent on the presence of a 5' phosphate or a 5' or 3' overhang, dsDNA fragments were treated either with T4 polynucleotide kinase (PNK), calf intestinal alkaline phosphatase (CIP), or restriction enzymes (Ndel, Notl, or Kpnl) as indicated (Figure 5-figure supplement 2A and D). With any of these modifications and similar to the parent, blunt dsDNA, degradation was only observed in combination of the absence of NaCl and presence of Mn²⁺ ions. To rule out double-stranded substrate length dependence, we assessed whether NrnC_{Bh} is capable of degrading annealed 27-nucleotide-long dsDNA or dsRNA with either a 5' or 3' overhang. Under conditions at which NrnC_{Bh} cleaves pGG within a minute (Figure 5A), no activity against double-stranded oligonucleotides was observed (Figure 5-figure supplement 2 and Figure 5—figure supplement 3). Blunt plasmid DNA and 27 bp DNA with a 5' or 3' overhang also failed to affect pGG degradation by NrnC_{8h} to an appreciable level, indicating that dsDNA does not act as an inhibitor of NrnC activity (Figure 5-figure supplement 3D). Finally, we compared the enzyme's activity against diribonucleotides pGG and pAA to that against deoxy-dinucleotide pdAdA or a single-stranded DNA trinucleotide, pdAdGdG. NrnC_{Bh} phosphodiesterase activity on diribonucleotides was sequence independent, with both pGG and pAA being processed following similar kinetics (Figure 5—figure supplement 3E). This result correlates with the structural analysis that revealed similar binding poses of these substrates at NrnC's active site (Figure 1—figure supplement 3). NrnC also cleaved pdAdA, nano-DNA with 2 nucleotides in length, at the same rate as diribonucleotides of the same sequence (Figure 5—figure supplement 3E). As was observed with RNA substrates, singlestranded DNA with more than two nucleotides were appreciably poorer substrates (Figure 5—figure supplement 3E).

Together, these experiments call into question a general DNase activity of NrnC, especially against dsDNA, although such an activity under specific cellular conditions remains plausible. Conversely, the studies indicate NrnC as a general dinuclease that cleaves deoxy-dinucleotides or diribonucleotides, a distinction to Orn and Rexo2 that act preferentially on diribonucleotides (*Nguyen et al., 2000*; *Mechold et al., 2006*; *Chu et al., 2019*). The functional relevance of an octameric NrnC assembly remains not fully understood. From the structural analysis, lateral subunit interactions within the octamer block off the active site at the 3' end of the substrate (*Figure 1*), consistent with 3'–5' exonuclease activity of the enzyme. But it is also possible that the octamer creates a nano-compartment for the efficient attraction and degradation of the smallest nano-RNase fragments, dinucleotides, with the central channel acting as a steric constriction for longer substrates.

Phylogenetic analysis indicates repeated evolution of critical dinuclease activity

After having elucidated the mechanisms that signify NrnC-type and Orn-type RNases as dedicated dinucleases, we reinvestigated the evolutionary distribution of these enzymes, relative to their structural homologs RNase D and RNase T, respectively. We included NrnA and NrnB in this analysis as the only other general RNases unrelated to NrnC and Orn, which also could stand in for Orn in a P. aeruginosa deletion strain, as shown previously (Orr et al., 2018). We identified homologs of the aforementioned proteins in the full UniprotKB database (version 2020 03), correlated the appearance of homologs in each species, and used the results to identify the spread of each type of nuclease at the order level (Figure 6). Orn was widespread in all eukaryotic groups, although in bacteria it was infrequently found outside of the Proteobacteria and Actinobacteria phyla. The structurally related RNase T is largely limited to Proteobacteria, with a few exceptions. Of the other major nucleases included in this analysis, NrnA was most frequently found in many bacteria. In contrast, NrnB occurs more sparsely distributed, potentially suggesting a more specialized function in individual organisms. NrnC is primarily found in most Alphaproteobacteria and Cyanobacteria, often overlapping with the occurrence of the homologous RNase D (with respect to the catalytic-domain sequence), although RNase D is present in many more bacterial genomes than NrnC. The three proteins that act as effective diribonucleases (Orn, NrnC, NrnA/NrnB) were largely – although not always – mutually exclusive; most bacterial taxa in this analysis had only one of the three, with the notable exception of Actinobacteria that frequently contained both Orn and NrnC (Figure 6).

We used the identified sequences of DnaQ family ribonucleases, each family curated individually, to create multiple sequence alignments and ultimately a combined phylogenetic tree of representative sequences of Orn, RNase T, NrnC, and RNase D family proteins (Figure 7). Similar to a previous



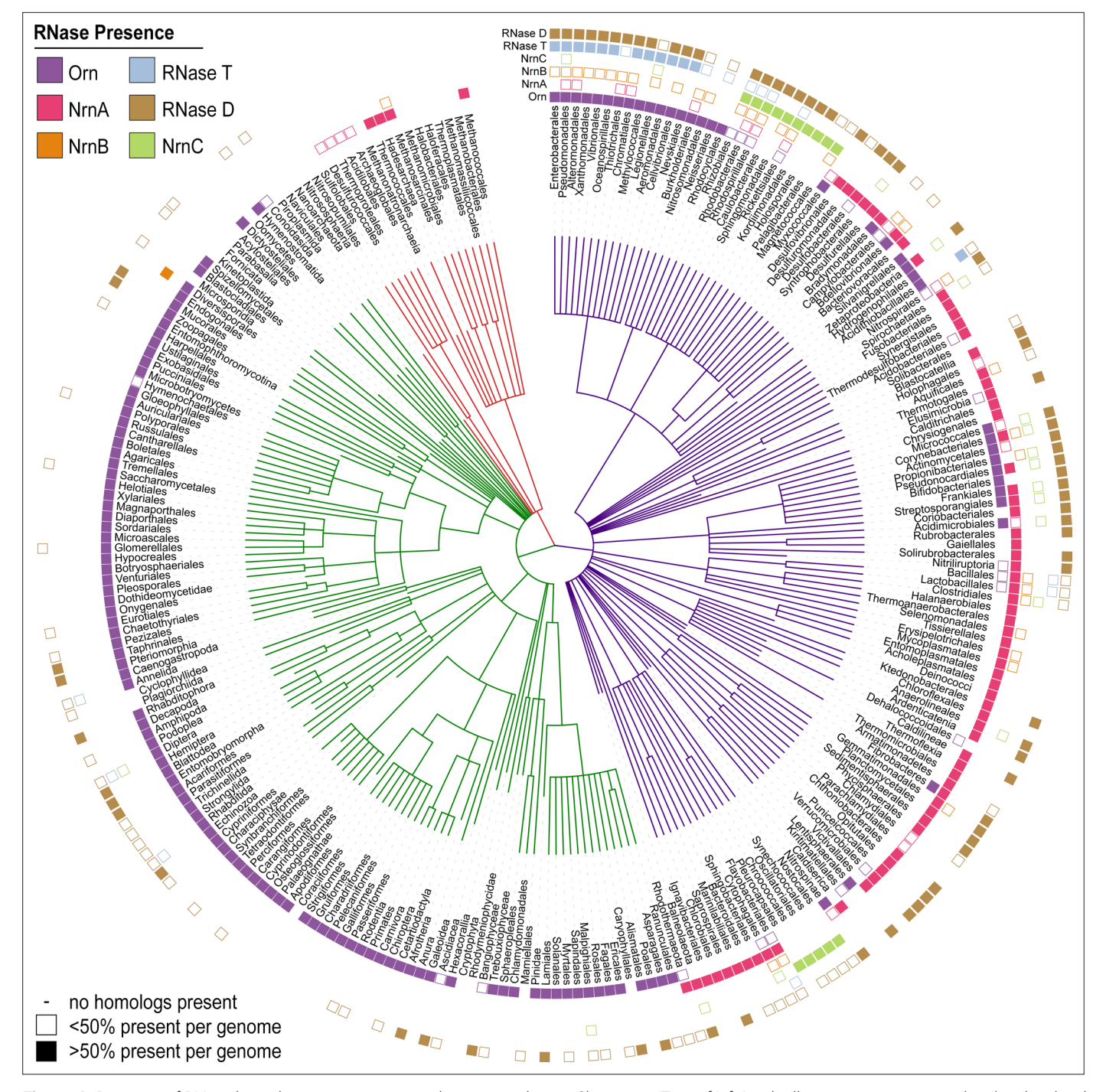


Figure 6. Presence of RNase homologs across sequenced organism classes. Shown is a 'Tree of Life' with all taxonomic groups at the class level with at least one substantially complete proteome available in the dataset. The tree is based on the structure of the NCBI Taxonomy database, with bacterial taxa shown with purple lines, eukaryotic taxa shown with green lines, and archaeal taxa shown with red lines. The presence of each RNase homolog as a proportion of the total proteins in that taxonomic group is shown as either a filled square (>50% presence of a homolog per genome) or an empty square (<50% presence of a homolog per genome). Lack of a square indicates no homologs for that family were present in genomes of that class.

analysis (*Zuo and Deutscher, 2001*), the DEDDh sequences (Orn and RNase T) segregated from the DEDDy sequences (RNase D and NrnC), highlighting the distinct evolutionary background of NrnC and Orn. Emanating from the ancestorial sequence, the first branch separated RNase T and Orn from RNase D and NrnC. This ancient split was soon followed by a split between RNase T and Orn. In the other lineage, NrnC and RNase D diverged from each other after a longer effective evolutionary time,



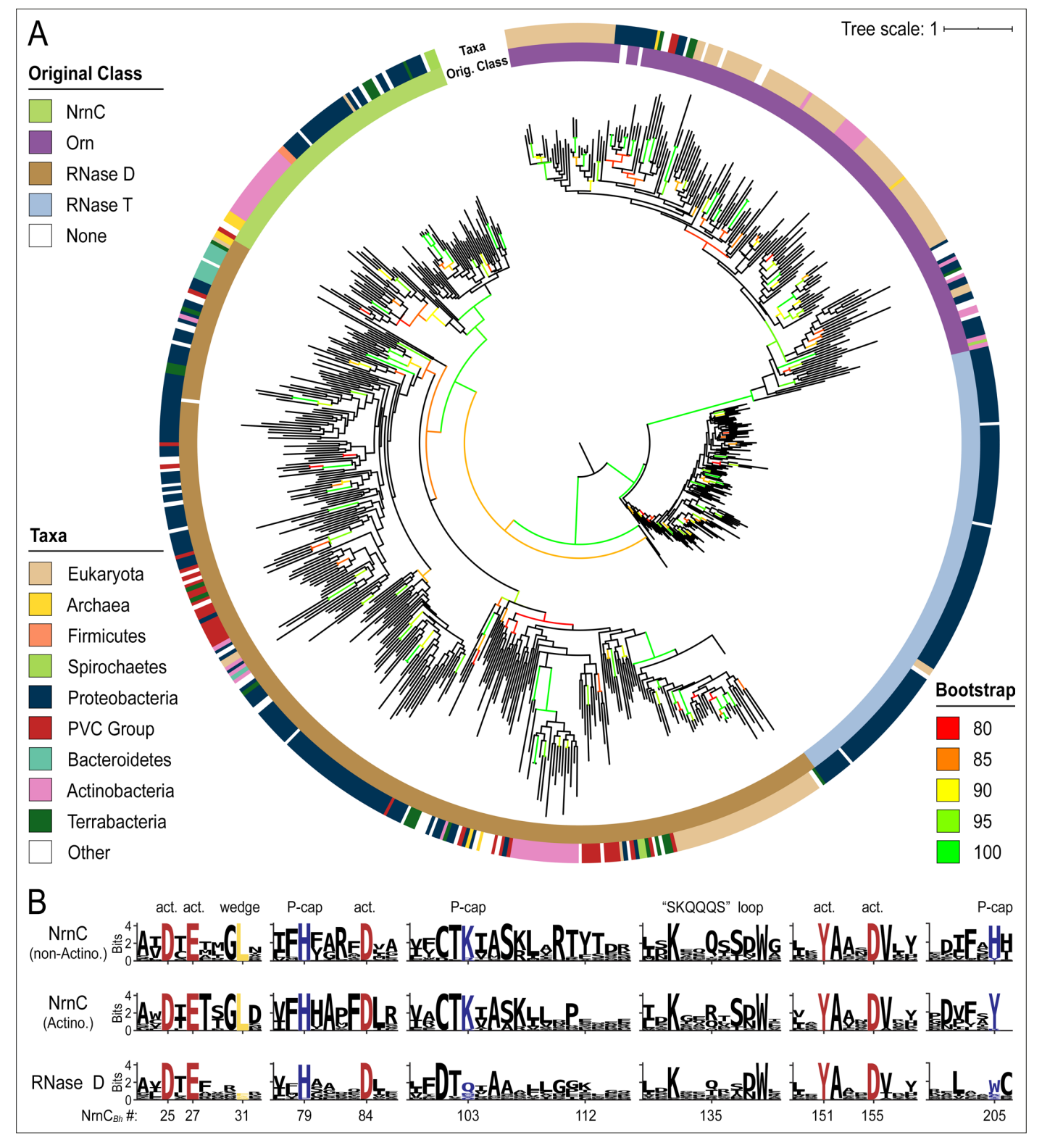


Figure 7. Phylogenetic tree of four DnaQ-fold RNase families. (**A**) Phylogenetic tree of 669 representatives of the RNase T, RNase D, oligoribonuclease (Orn), and nano-RNase C (NrnC) families of RNase proteins. The inner ring represents the original classification of each sequence by HMM analysis. The outer ring represents the high-level taxonomic classification of the organism the protein is found in. The color of the branch represents the UFBoot bootstrap value, where black branches are <80%, red is 80%, orange is 85%, yellow is 90%, light green is 95%, and bright green is 100%. Bootstrap values > 90% indicate high-confidence splits. (**B**) Sequence logos of RNase D and NrnC subgroups. Sequence logos showing the relative entropy (information content) at selected positions in RNase D as well as the Actinobacterial and non-Actinobacterial subsets of NrnC. Sequence numbering is relative to *Bartonella birtlessi* NrnC (G4VUY7). Active site residues are shown in red, phosphate cap residues in dark blue, and the L-wedge in yellow.



presumably following a duplication from the more closely related RNase D (*Figure 7A*). Due to this relatively recent split, and as it frequently co-occurs with RNase D, NrnC appears to have arisen from a more recent specialization event.

Catalytic, L-wedge, and phosphate cap residues are strictly conserved in many NrnC orthologs (*Figures 1D and 7B*). RNase D, the closest relative to NrnC, shares the catalytic DEDDy motif with NrnC, but lacks the L-wedge and phosphate cap (*Figure 7B*), suggesting that these features distinguish NrnC (and Orn) from other RNases and DnaQ-fold enzymes. The phylogenetic analysis also identified a unique group of NrnC-like enzymes in Actinobacteria, which shares most of the characteristic NrnC features, including conservation of the active site, most of the phosphate cap and wedge residues. However, subtle but specific changes in important residues (i.e., a Q-to-R change in the SKQQQS loop and the phosphate cap's H²⁰⁵, which is replaced by a tyrosine residue) hint at the possibility of distinct function of the NrnC orthologs in this subgroup (*Figure 7*). Some Actinobacteria also encode an additional Orn and/or NrnA in the same genome, which could suggest either redundant functions or further specialization of these enzymes in these organisms (*Figure 6*).

Conclusions

The establishment of NrnC as a dedicated dinuclease led us to compare and contrast the structural features of NrnC and Orn, the other enzyme with such a specific activity (*Kim et al., 2019*). Because

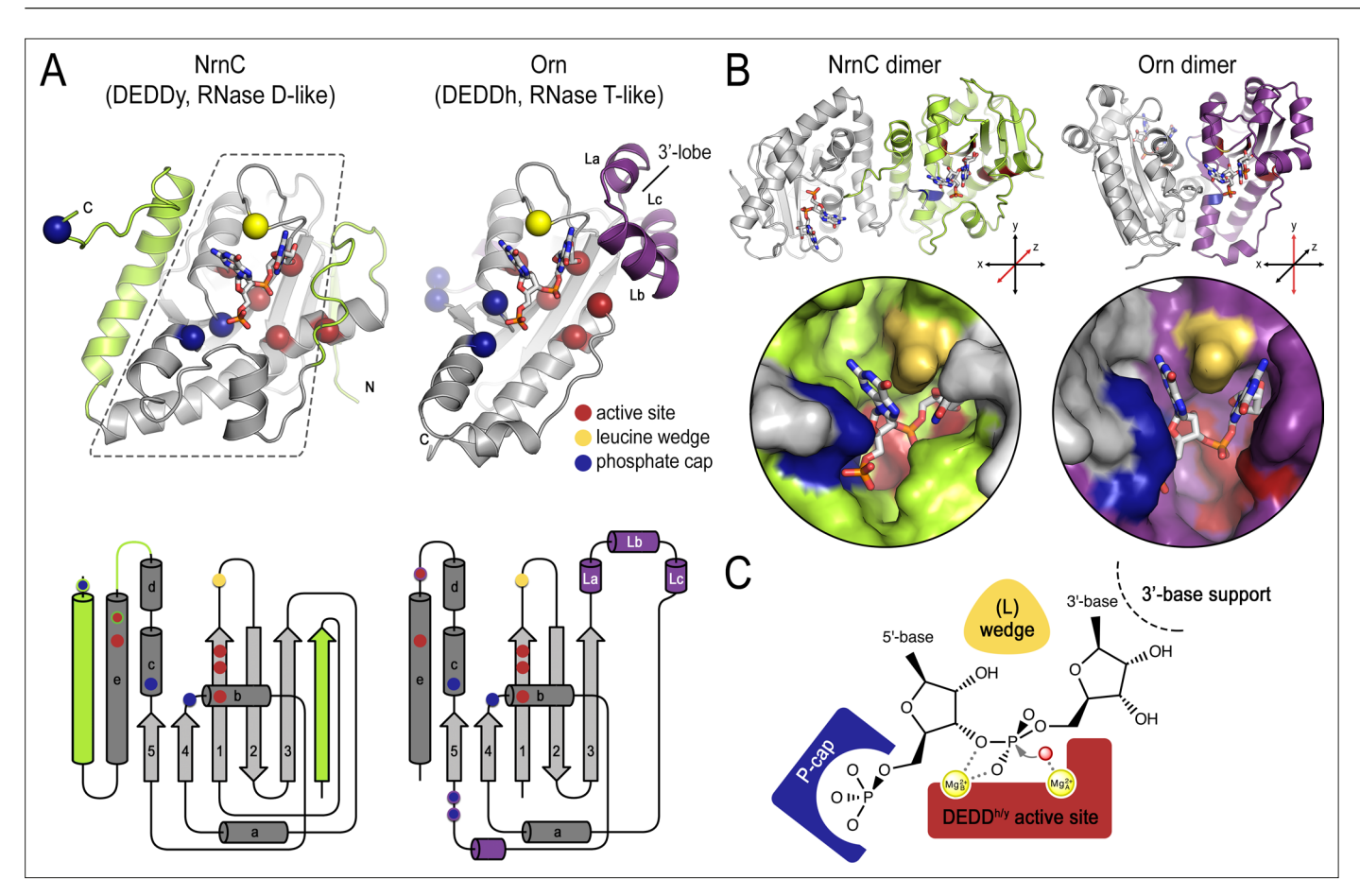


Figure 8. Structural comparison of nano-RNase C (NrnC) and oligoribonuclease (Orn). (A) Fold topology. pGG-bound NrnC and Orn monomers are shown in a similar orientation as cartoons (top) or schematic topology diagrams (bottom). Conserved catalytic core elements are colored in gray. NrnC and Orn-specific features are colored in green and purple, respectively. Other color codes mark the positions of the DEDDy/h motif (red spheres), L-wedge (yellow sphere), and phosphate cap residues (dark blue spheres). (B) Comparison of dimer units of NrnC and Orn (top) with close-ups of the composite active sites of the enzymes (bottom). An NrnC monomer is colored green and an Orn monomer is colored purple, with adjacent monomers in the biological assemblies colored in light gray. Specific residues are colored as in (A). Coordinate systems indicate the twofold symmetry axis of the enzyme dimers, with the colored monomers shown in a similar orientation. (C) Structurally and functionally conserved features common among NrnC-and Orn-type diribonucleases.



NrnC and Orn evolved independently from two different families of RNases, RNase D and RNase T, respectively, their shared substrate length specificity is particularly noteworthy. On the level of a single subunit, NrnC and Orn contain a conserved catalytic core comprising a β -sheet and adjacent α -helices, which harbors the residues for divalent cation coordination, the functionally important tyrosine or histidine residue ('DEDDy' or 'DEDDh'), and a wedge residue (L-wedge) that separates the substrate's bases (*Figure 8A*). In addition, the position of two residues contributing to the respective phosphate caps is conserved, but the identity of the residues varies between the two enzyme groups. For both enzyme families, the active site involves residues from two monomers requiring minimally a dimeric protein (*Figure 8B*). Thus, the two enzyme families are characterized by a functionally conserved active site optimized to accommodate the shortest RNA substrates, which distinguishes the dinucleases characterized to date from other RNases that act on longer substrates.

Despite these remarkable, function-defining commonalities between NrnC and Orn/Rexo2, their different evolutionary histories have led to distinct implementation of some of these important features. Particularly, NrnC and Orn differ in secondary structure motifs at the periphery of their conserved catalytic core. The enzyme family-specific parts include, for NrnC, additional phosphate cap residues, an N-terminal β -strand, and an additional C-terminal α -helix; and for Orn, short helices La, Lb, and Lc forming a lobe that coordinates the 3' base of the dinucleotide substrate (Figure 8A). On the quaternary structure level, both NrnC and Orn form dimers (Figure 8B). However, the specific dimer arrangements vary between NrnC and Orn. The C-terminal α -helix of NrnC, which is absent in Orn, serves as the major dimerization interface in this family of enzymes, yielding a twofoldsymmetric dimer. Orn and Orn-related enzymes (such as Rexo2) also form a twofold symmetric unit, but via a distinct rotation axis and the interface involves elements of the central core fold (Figure 8B). In contrast to Orn/Rexo2, whose biological unit is the dimeric form, four dimers of NrnC assemble further to the final octameric assembly. Lateral interfaces between dimers of NrnC within the octamer replace the 3' lobe of Orn in coordinating the 3' base of the substrate. Despite these major differences in the architectural composition and unique features of the two enzyme families, the elements that we identified as characteristic for dinucleases align nearly perfectly in space (Figure 8B and C).

Of the NrnC-specific motifs, the N-terminal β -strand and near-C-terminal α -helix are conserved in RNase D (*Figure 1—figure supplement 2B*). NrnC's C-terminal extension including H²⁰⁵, placed in the active site of an adjacent subunit within a NrnC dimer, is involved in 5' base stacking and completes the phosphate cap. Mutations in NrnC's unique phosphate cap retained residual activity, suggesting a role mainly in restricting the length of substrates accommodated at the active site (*Figure 2*). In contrast, corresponding mutations at the phosphate cap of Orn abolished catalytic activity, suggesting that these residues contribute directly to the catalytic mechanism in addition to imposing a substrate length restriction at the active site (*Kim et al., 2019*). One possibility is that the more ancient Orn evolved more stringent diribonucleotide preference compared to the more recently occurring NrnC-type enzymes. Taken together, the phosphate cap is a unifying feature of Orn and NrnC, though arisen independently in the two enzyme classes. In general, evolution of such specialized active sites that only degrade dinucleotides would also allow for rapid turnover of this specific nucleotide pool since competition from longer RNAs (or DNAs) would be suppressed. Whether similar motifs have evolved in other enzymes to restrict substrate length remains to be established.

Together, our bioinformatics analysis revealed the unique histories of NrnC and Orn, two nucleases that arose independently to fulfill the crucial role of dinucleotide degradation. Their activities are at the confluence of RNA metabolism and bacterial second messenger signaling, signifying their importance for cellular homeostasis and regulation. Indeed, functional NrnC or Orn, and consequently the clearance of the cellular dinucleotide pool, are necessary for proper growth, being essential in many organisms (*Ghosh and Deutscher, 1999; Kim et al., 2019; Liu et al., 2012; Sternon et al., 2018*), which could provide an avenue for targeted antimicrobial intervention. Specifically, as *Bartonella* and *Brucella* species are important pathogens (*Dehio, 2005; Greenfield et al., 2002; Pappas et al., 2006*), understanding the implications of NrnC function and failure could offer insight and effective strategies to battle the pernicious impacts of these organisms. Our structure-function studies present blueprints for such endeavors by revealing the specific active-site architectures and activity profiles of NrnC and Orn/Rexo2, their similarities and differences, as well as the general features that distinguish dinucleases from other 3'–5' exonucleases.



Materials and methods

Key resources table

Reagent type (species) or resource	Designation	Source or reference Identifiers	Additional information
Strain, strain background			
(Pseudomonas aeruginosa)	PA14	Rahme et al., 1995 ; PMID:7604262	
Strain, strain background (<i>P.</i>			
aeruginosa)	PA14 ∆orn	This study	
Strain, strain background			
(Escherichia coli)	Stellar cells	Takara/Clontech	
Strain, strain			
background (E. coli)	BL21(DE3)	New England Biolabs	
	· , ,	DIOIADS	
Recombinant DNA reagent	pEX-Gn-Δ <i>orn</i> (plasmid)	This study	
Recombinant DNA		Newman and Fuqua, 1999;	
reagent	pJN105 (plasmid)	PMID:10023058	
Recombinant DNA		Kim et al., 2019;	
reagent	pJHA (plasmid)	PMID:31225796	

Continued on next page



Reagent type Additional (species) or Source or reference Identifiers resource Designation information ACAGATTGGTGGATC CATGACCGAAATTCGCG TGCATCAGGGCGATCTGC CGAACCTGGATAACTAT CGCATTGATG CGGTGGCG **GTGGATACCG** AAACCCTGG GCCTGCAGCC GCATCGCGAT CGCCTGTGCG TGGTGCAGCTG AGCAGCGGCGA TGGCACCGC **GGATGTGATTCA** GATTGCGAA AGGCCAGAAAA GCGCGCCGAA CCTGGTGCGCC TGCTGAGCG **ATCGCGATATT** ACCAAAATTTTT CATTTTGGCCGC TTTGATCTG GCGATTCTGGCG CATACCTTTG GCGTGATGCCG GATGTGGTGT TTTGCACCAAAAT TGCGAGCAA ACTGACCCGCAC CTATACCGATCGC CATGGCCTGAAAG AAATTTGCGG CGAACTGCTGAAC GTGAACATTAG CAAACAGCAGCAG AGCAGCGATTG GGCGGCGGAAAC CCTGAGCCGCG CGCAGATTGAATAT GCGGCGAGCG ATGTGCTGTATCTG CATCGCCTGAA AGATATTTTTGAAG AACGCCTGAAA CGCGAAGAACGCG AAAGCGTGGCG AAAGCGTGCTTTC AGTTTCTGCCGA TGCGCGCGAACC TGGATCTGCTGG GCTGGAGCGAAATTG Custom DNA ATATTTTTGCG fragment for CATAGCTAAGCGGC Bartonella henselae NrnC, cloned in to His₆-SUMO-pET28 Sequence-based CGCACTCGAGCA (DNA fragment) BH02530 Geneart reagent

Continued

Continued on next page



Reagent type

Continued

Additional (species) or Source or reference Identifiers resource Designation information ACAGATTGGTG GATCCATGACCA TTCGCTTTCATC GCAACGATCT GCCGAACCTGGA TAACTATCAGG TGGATGCGGTG GCGATTGATAC CGAAACCCTGG GCCTGAACCCGC ATCGCGATCGCC TGTGCGTGGTG CAGATTAGCCCG GGCGATGGCAC CGCGGATGTGA TTCAGATTGAAGC GGGCCAGAAAAA GCGCCGAACC TGGTGAAACTGC TGAAAGATCGC **AGCATTACCAAAA** TTTTTCATTTTG GCCGCTTTGATC TGGCGGTGCTG GCGCATGCGTTT GGCACCATGCC **GCAGCCGGTGTT** TTGCACCAAAAT **TGCGAGCAAACTG** ACCCGCACCT ATACCGATCGCCAT **GGCCTGAAAG** AAATTTGCAGCGA ACTGCTGGATG TGAGCATTAGCAA ACAGCAGCAG AGCAGCGATTGGG CGGCGGAAG TGCTGAGCCAGG CGCAGCTGGAA TATGCGGCGAG CGATGTGCTGTAT CTGCATCGCCTG AAAGCGGTGCT GGAACAGCGCCT **GGAACGCGAT** GGCCGCACCAAA CAGGCGGAAGC GTGCTTTAAATTT CTGCCGACCCG CAGCGAACTGGA TCTGATGGGCTG Custom DNA GGCGGAAAGCGA fragment for Brucella TATTTTTGCGCAT melitensis NrnC, Sequence-based AGCTAAGCGGCCGCACTC cloned in to His,reagent GAGCA (DNA fragment) Geneart **BMEI1828** SUMO-pET28 Recombinant DNA His,-SUMO-pET28-Cloned from custom NrnC_{Bh} (plasmid) This study DNA fragment reagent Recombinant DNA His6-SUMO-pET28-Cloned from custom reagent $NrnC_{Bm}$ (plasmid) This study DNA fragment NrnC_{Bh} cloned into Recombinant DNA pJHA for expression pJHA- $NrnC_{Bh}$ (plasmid) in P. aeruginosa This study reagent $NrnC_{Bm}$ cloned into pJHA for expression Recombinant DNA in P. aeruginosa pJHA-NrnC_{Bm} (plasmid) This study reagent Product of site-directed Continued on next page Recombinant DNA pJHA-NrnC_{Bh} mutagenesis of reagent D25A (plasmid) This study pJHA-NrnC_B



Reagent type (species) or		Continued	Additional
esource	Designation	Source or reference Identifiers	information
Recombinant DNA eagent	pJHA-NrnC _{Bh} E27A (plasmid)	This study	Product of site-directed mutagenesis of pJHA-NrnC _{Bh}
Recombinant DNA reagent	pJHA-NrnC _{Bh} D84A (plasmid)	This study	Product of site-directed mutagenesis of pJHA-NrnC _{Bh}
Recombinant DNA reagent	pJHA-NrnC _{Bh} D155A (plasmid)	This study	Product of site-directed mutagenesis of pJHA-NrnC _{Bh}
Recombinant DNA reagent	pJHA-NrnC _{Bh} Y151A (plasmid)	This study	Product of site-directed mutagenesis of pJHA-NrnC _{Bh}
Recombinant DNA eagent	pJHA-NrnC _{Bh} L31A (plasmid)	This study	Product of site-directed mutagenesis of pJHA-NrnC _{Bh}
Recombinant DNA reagent	pJHA-NrnC _{Bh} H79A (plasmid)	This study	Product of site-directed mutagenesis of pJHA-NrnC _{Bh}
Recombinant DNA reagent	pJHA-NrnC _{Bh} K103A (plasmid)	This study	Product of site-directed mutagenesis of pJHA-NrnC _{Bh}
Recombinant DNA reagent	pJHA-NrnC _{Bh} H205A (plasmid)	This study	Product of site-directed mutagenesis of pJHA-NrnC _{Bh}
Recombinant DNA reagent	pJHA-NrnC _{Bh} K132A (plasmid)	This study	Product of site-directed mutagenesis of pJHA-NrnC _{Bh}
Sequence-based reagent	TTTGGGCTAGCCA TATGACCGAAATT CGTGTTCATCAGGG	NrnC _{Bh} Life Technologies infusionprimer	Primer for cloning _F NrnC _{Bh} into pJHA
Sequence-based reagent	GCTCAAGCTTGAAT TCGCTGTGTGCAA AGATATCAATTTCG	NrnC _{Bh} _ Life Technologies infusionprimer	Primer for cloning _R NrnC _{Bh} into pJHA
Sequence-based reagent	TTTGGGCTAGCCA TATGACCATTCGTT TTCATCGTAATGATC	NrnC _{Bm} _ Life Technologies infusionprimer	Primer for cloning _F NrnC _{Bm} into pJHA
Sequence-based reagent	GCTCAAGCTTG AATTCGCTATGTG CAAAAATATCGCTTT	NrnC _{Bm} _ Life Technologies infusionprimer	Primer for cloning _R NrnC _{Bm} into pJHA
Sequence-based reagent	Acccagtgtttcggtagc aacggcaactgcatc	Life Technologies NrnC _{Bh} D25A_c	Primer for site directed mutagenesis
Sequence-based reagent	Gatgcagttgccgttgct accgaaacactgggt	Life Technologies NrnC _{Bh} D25A_I	Primer for site directed mutagenesis
Sequence-based reagent	Gttgccgttgataccgca acactgggtctgcag	Life Technologies NrnC _{Bh} E27A_e	Primer for site directed mutagenesis
Sequence-based reagent	Ctgcagacccagtgttgc ggtatcaacggcaac	NrnC _{Bh} Continued on next life Jechnologies E27A_b	Primer for site directed mutagenesis



Reagent type (species) or resource	Continued Designation	Source or reference	Identifiers	Additional information
Sequence-based reagent	Cgatgcggctgcgcac ccagtgtttcggtatcaacg	Life Technologies	NrnC _{Bh} L31A_a	Primer for site directed mutagenesis
Sequence-based eagent	Cgttgataccgaaaca ctgggtgcgcagc cgcatcg	Life Technologies	NrnC _{Bh} L31A_b	Primer for site directed mutagenesis
Sequence-based reagent	Agatcgaaacgacca aaggcaaagattttg gtaatatcacgatcgc	Life Technologies	NrnC _{Bh} H79A_a	Primer for site directed mutagenesis
Sequence-based reagent	Gcgatcgtgatattacc aaaatctttgcctttg gtcgtttcgatct	Life Technologies	NrnC _{Bh} H79A_b	Primer for site directed mutagenesis
Sequence-based reagent	Gtgccagaattgccag agcgaaacgac caaagtga	Life Technologies	NrnC _{Bh} D84A_a	Primer for site directed mutagenesis
Sequence-based reagent	Tcactttggtcgtttcgct ctggcaattctggcac	Life Technologies	NrnC _{Bh} D84A_b	Primer for site directed mutagenesis
Sequence-based reagent	Cgggtcagtttgcttgc aattgcggtacaa aaaacaacatccgg	Life Technologies	NrnC _{Bh} K103A_a	Primer for site directed mutagenesis
Sequence-based reagent	Ccggatgttgttttttgtacc gcaattgcaagca aactgacccg	Life Technologies	NrnC _{Bh} K103A_b	Primer for site directed mutagenesis
Sequence-based reagent	Acatcacttgctgcagct tcaatctgtgcac ggctcagg	Life Technologies	NrnC _{Bh} Y151A_a	Primer for site directed mutagenesis
Sequence-based reagent	Cctgagccgtgcacag attgaagctgca gcaagtgatgt	Life Technologies	NrnC _{Bh} Y151A_b	Primer for site directed mutagenesis
Sequence-based reagent	Cggtgcagatacaga acagcacttgctgcatattcaa	Life Technologies	NrnC _{Bh} D155A_a	Primer for site directed mutagenesis
Sequence-based reagent	Ttgaatatgcagcaag tgctgttctgtatctgcaccg	Life Technologies	NrnC _{Bh} D155A_b	Primer for site directed mutagenesis
Sequence-based reagent	Gctcaagcttgaattc gctggctgcaa agatatcaatttcgc	Life Technologies	NrnC _{Bh} H205A_a_pJHA	Primer for site directed mutagenesis
Sequence-based reagent	Gcgaaattgatatctttgc agccagcgaattcaagcttgagc	Life Technologies	NrnC _{Bh} H205A_b_pJHA	Primer for site directed mutagenesis
Sequence-based reagent	Gtgcggccgcttagctgg ctgcaaagatatcaatttcgct	Life Technologies	NrnC _{Bh} H205A_a_SUMO	Primer for site directed mutagenesis
Sequence-based reagent	Agcgaaattgatatcttt gcagccagctaa gcggccgcac	Life Technologies	NrnC _{Bh} H205A_b_SUMO	Primer for site directed mutagenesis
Sequence-based reagent	5'-GG-3' (RNA primer)	Sigma		
Sequence-based reagent	5'-AGG-3' (RNA primer)	Sigma		
Sequence-based reagent	5'-AAGG-3' (RNA primer)	Sigma		
	5'-AAAGG-3'			
Sequence-based reagent	(RNA primer)	Sigma		



Reagent type (species) or	Darianativa	Continued	C	I danatif	Additional
resource	Designation		Source or reference	Identifiers	information
Sequence-based reagent	5'-AAAAAGG-3' (RNA primer)		Sigma		
Sequence-based reagent	5'-pGG-3' (RNA prime	-)	Biolog' catalog number P023-01		
Sequence-based reagent	5'-pAA-3' (RNA primer)	Biolog' catalog number P033-01		
Sequence-based reagent	5'-pGC-3' (RNA primer)	GE Healthcare Dharmacon		
Chemical compound, drug	5'-pAp-3' (RNA primer))	Sigma	Cat# A5763	
Sequence-based reagent	Various RNA and DNA oligonucleotides		IDT		
Antibody	Anti-HA (rabbit polyclonal)		Takara	Cat# 631207	(1:100)
Antibody	Anti-HA-agarose (mouse monoclonal, clone HA-7)		Sigma	Cat# A2095; RRID:AB_257974	(10 µl)
Antibody	Anti-rabbit (donkey polyclonal, HRP-conjugated)		Cytiva	Cat# NA934	(1:5000)
Software, algorithm	Prism		GraphPad	RRID:SCR_002798	
Software, algorithm	XDS Program Package		Kabsch, 2010 ; PMID:20124693	RRID:SCR_015652	Distributed through SBGrid
Software, algorithm	Pointless		Evans, 2006 ; PMID:16369096	RRID:SCR_014218	Distributed through SBGrid
Software, algorithm	Scala		Evans, 2006 ; PMID:16369096		Distributed through SBGrid
Software, algorithm	Phenix		Adams et al., 2010 ; PMID:20124702	RRID:SCR_014224	Distributed through SBGrid
Software, algorithm	Coot		Emsley et al., 2010 ; PMID:20383002	RRID:SCR_014222	Distributed through SBGrid
Software, algorithm	MrBump		Keegan et al., 2018 ; PMID:29533225		Distributed through SBGrid
Software, algorithm	PyMOL		Schrödinger	RRID:SCR_000305	Distributed through SBGrid
Software, algorithm	UCSF ChimeraX		Pettersen et al., 2021 ; PMID:32881101	RRID:SCR_015872	Distributed through SBGrid
Software, algorithm	cryoSPARC		Punjani et al., 2017 ; PMID:28165473	RRID:SCR_016501	
Software, algorithm	RELION		Zivanov et al., 2018 ; PMID:30412051	RRID:SCR_016274	
Software, algorithm	GCTF		Zhang, 2016 ; PMID:26592709	RRID:SCR_016500	
Software, algorithm	iTOL		Letunic and Bork, 2019 ; PMID:30931475	RRID:SCR_018174	
Software, algorithm	TCoffee	Continued on next	Notredame et al., 2000; PMDe 10964570	RRID:SCR_019024	
Software, algorithm	Hmmer		Eddy, 2011 ; PMID:22039361	RRID:SCR_005305	



Reagent type (species) or resource	Designation	Continued Source or reference Identifiers	Additional information
Software, algorithm	MAFFT	Katoh et al., 2005 ; PMID:15661851 RRID:SCR_011811	
Software, algorithm	SnakeMake	Köster and Rahmann, 2018; PMID:29788404 RRID:SCR_003475	

Expression constructs and mutagenesis

For protein expression in *Escherichia coli*, codon-optimized NrnC genes from *B. henselae* (BH02530) and *B. melitensis* (BMEI1828) were synthesized by Geneart (Life Technologies). Genes were cloned into a modified pET28a vector (Novagen) between BamHI and NotI sites using InFusion cloning (Takara Bio). The resulting fusion proteins expressed from these plasmids contained an N-terminal His₆-tagged small ubiquitin-like modifier (SUMO) cleavable by recombinant Ulp-1 protease.

For the arabinose-inducible expression and detection of NrnC in *P. aeruginosa*, we used a modified pJN105 vector (**Newman and Fuqua**, **1999**). The vector pJGHA was constructed by inserting a coding sequence for monomeric superfolder GFP (msfGFP)-HA epitope fusion between the Nhel and Xbal sites in pJN105. The plasmid allows insertion of genes of interest between novel Ndel and EcoRI sites, and their expression results in proteins with C-terminal msfGFP-HA. The vector pJHA was constructed by digesting pJGHA with HindlII (New England Biolabs) to remove the msfGFP coding sequence. Following re-ligation of the gel-purified restriction digest, the coding sequence for the HA epitope remained, allowing proteins of interest to be expressed with a C-terminal HA epitope.

For expression in *P. aeruginosa*, the codon-optimized NrnC_{Bh} sequences were amplified by PCR and inserted between Ndel and EcoRI sites of the pJHA vector using InFusion cloning.

A QuikChange II site-directed mutagenesis kit (Agilent) was used for the introduction of point mutations in *nrnc_{Bh}* following the manufacturer's instructions. All mutations were verified by DNA sequencing.

Protein expression and purification

E. coli BL21 T7 Express cells (New England Biolabs) were transformed with pET28a plasmids encoding His_6 -SUMO-NrnC_{Bh} or -NrnC_{Bm} and grown in Terrific Broth (TB) supplemented with 50 µg/ml kanamycin at 37 °C to an OD₆₀₀ of ~1.0. Induction was carried out at 18 °C with 0.5 mM IPTG for 16 hr. Cells were harvested by centrifugation, resuspended in minimal volume of Ni-NTA binding buffer (25 mM Tris-Cl pH 8.5, 500 mM NaCl, 20 mM imidazole), frozen in liquid nitrogen, and stored at –80 °C.

Cell pellets were thawed followed by lysis through sonication and centrifugation. Supernatants were incubated on ice with Ni-NTA resin (Qiagen) equilibrated with Ni-NTA binding buffer for 1 hr with gentle agitation. The NrnC-bound resin was washed three times with 10 column volumes of Ni-NTA binding buffer by gravity flow. Bound NrnC was eluted in six-column volumes of Ni-NTA elution buffer (25 mM Tris-Cl pH 8.5, 500 mM NaCl, 400 mM imidazole). Eluates were buffer exchanged into gel filtration buffer (25 mM Tris-Cl, 150 mM NaCl, pH 7.5) via a HiPrep 26/10 desalting column (GE Healthcare) and incubated overnight with Ulp-1-His₆ to cleave the His₆-tagged SUMO moiety from NrnC. Following Ulp-1 cleavage, untagged NrnC protein was recovered in the flow through of a HisTrap Ni-NTA column (GE Healthcare), separated from His₆-SUMO, and ULP1-His₆. EDTA at a final concentration of 10 mM was added to NrnC before concentration via an Amicon Ultra 10K concentrator (Merck Millipore). Concentrated NrnC was injected onto a HiLoad 16/60 Superdex 200 gel filtration column (GE Healthcare) equilibrated in gel filtration buffer. Fractions containing NrnC were concentrated, frozen in liquid nitrogen, and stored at –80 °C.

Crystallization, data collection, and structure refinement

NrnC-RNA complexes (pGG and pAA from Biolog Life Science Institute, other nucleotides from Dharmacon) were formed prior to crystallization by mixing 1:2 molar ratio of protein:nucleotide in gel filtration buffer, followed by 30 min incubation at the crystallization temperature. Protein concentrations used in crystallization ranged from 2.5 to 10 mg/ml (NrnC_{Bh}) and 1.0 to 8.0 mg/ml (NrnC_{Bm}). Crystals were grown via hanging-drop vapor diffusion by mixing equal volumes (0.8 μ l) of sample with reservoir solution. NrnC_{Bh} crystals grew at 20 °C over a reservoir solution containing 0.1 M succinic acid (pH 6.5), 15–20% PEG 3350, and 20% xylitol. NrnC_{Bm} crystals grew at 4°C and 20°C, in reservoir



solutions containing 0.1 M Tris-Cl (pH 7), 2.0–2.4 M ammonium sulfate or 1.4 M sodium-potassium phosphate, and 20% xylitol. Prior to freezing crystals in liquid nitrogen, they were soaked in reservoir solution with up to 25% xylitol. Data were collected by synchrotron radiation on frozen crystals at Cornell High Energy Synchrotron Source (CHESS) and NE-CAT 24ID-C and 24ID-E beamlines at the Advanced Photon Source (APS) at Argonne National Laboratory. Diffraction data sets were processed using XDS, Pointless, and Scala (*Evans, 2006; Kabsch, 2010*). The initial structures were solved by molecular replacement using the software package Phenix (*Adams et al., 2010*) and MrBUMP in the ccp4 suite (*Keegan et al., 2018; Winn et al., 2011*) with the coordinates of *E. coli* RNase D (PDB:1yt3, *Zuo et al., 2005*) as the search model. Manual model building and refinement were carried out with Coot (*Emsley et al., 2010*) and Phenix. Illustrations were prepared in Pymol (version 2.0 Schrödinger, LLC). All software packages were accessed through SBGrid (*Morin et al., 2013*). All data collection and refinement statistics are summarized in *Supplementary file 1*.

Structure determination by cryo-EM

Purified NrnC_{Bh} was diluted in buffer (25 mM Tris-Cl pH 7.5, 150 mM NaCl) to 4, 5, or 6 mg/ml (for incubation with pGG, pAGG, and pAAAGG, respectively). RNA substrate was added at threefold molar excess. After 15 min at room temperature, NP40 was added at 0.01% v/v and samples were placed on ice for an additional 15 min. Alternatively, NrnC was diluted to 7.5 mg/ml and incubated with threefold excess pAAAGG; after 15 min, 1/5 volume of buffer with CaCl₂ and NP40 (25 mM Tris-Cl pH 7.5, 150 mM NaCl, 5 mM CaCl₂, 0.05% NP40) was added and incubations proceeded for another 15 min on ice. All cryo-EM samples were prepared with Quantifoil R1.2/1.3 300-mesh grids after glow discharging in a PELCO easiGlow (60 s glow, 10 mA current, 80% Ar/20% O₂) using a FEI Mark IV Vitrobot (4 °C, 100% humidity, 2.5 s blot) to plunge grids into liquid nitrogen-cooled ethane immediately after blotting. Data were collected using the Cornell CCMR facility Thermo Fisher Scientific Talos Arctica with a Gatan K3 detector and BioQuantum energy filter operated at 200 kV at a nominal magnification of 63 kX (1.24 Å/pixel), 20 eV slit width, and 0.5× binning (super-resolution). Movies were collected with a total dose of 50 e/Ų, fractionated into either 50 or 75 frames.

Data processing was performed using RELION 3.1 (Zivanov et al., 2018) and cryoSPARC (Punjani et al., 2017). Super-resolution movie exposures were aligned, dose-weighted, and Fourier-cropped to the physical pixel size in RELION using MotionCor2 (Zheng et al., 2017), and defocus values were estimated using GCTF (Zhang, 2016). Micrographs were then imported into cryoSPARC for manual curation, particle picking, and classification. Particles were picked using the cryoSPARC 'blob' and template picking and initially extracted with Fourier-cropping to a nominal pixel size of 2.89 Å. This particle stack was cleaned with 2D and 3D classifications in cryoSPARC, then re-extracted in RELION (1.24 Å/pixel) for 3D refinement, CTF refinement, and Bayesian polishing. Further 2D and 3D classification of CTF-refined particles in RELION was performed for the pAGG dataset. For each dataset, no symmetry was imposed during processing until a final refinement was performed imposing D4 symmetry. The crystal structure of NrnC_{Bh} was docked into the reconstructed cryo-EM density maps using the program package Phenix (Liebschner et al., 2019) and the models were refined in Coot (Emsley et al., 2010), ChimeraX (Pettersen et al., 2021), and the real-space refinement module for cryo-EM in Phenix (Afonine et al., 2018). Illustrations were prepared with ChimeraX and show the density of the sharpened maps. All data collection and refinement statistics are summarized in Supplementary file 2.

Complementation analysis in P. aeruginosa

Deletion of *orn* in *P. aeruginosa* UCBPP-PA14 was performed using two-step allelic exchange as described by Hmelo and colleagues (*Hmelo et al., 2015*). Briefly, deletion alleles were created by overlap extension PCR, and delivered on a pEX18 suicide plasmid to the *P. aeruginosa* host strain by conjugation with *E. coli* donor strain S17.1, leading to the removal of the gene from the genome. To test for complementation, genes were introduced into the *P. aeruginosa orn* deletion strains by using electroporation (*Choi et al., 2006*). Briefly, *P. aeruginosa* cells were grown overnight, centrifuged, then washed with and resuspended in 300 mM sucrose. Expression plasmids based on the pJHA vector were mixed with 100 µl of resuspended cells and electroporated using a Micropulser (Bio-Rad) followed by recovery in 1 ml of lysogeny broth (LB), shaking at 250 rpm for 1 hr at 37 °C. Recovered



cells were plated on LB plates containing 60 μ g/ml gentamicin. Individual colonies were used for subsequent experiments.

Drip assay

The indicated *P. aeruginosa* strains harboring expression plasmids were grown overnight with shaking at 37 °C in LB supplemented with 60 μ g/ml gentamicin. The cells were adjusted to CFU = 10,000 in fresh LB medium and applied to LB plates supplemented with 60 μ g/ml gentamicin and 0.2% arabinose in 20 μ l drops. The plates were inverted allowing the culture to drip down the length of the plate, followed by incubation overnight at 37 °C. The plates were imaged using a Chemidoc MP imager (Bio-Rad) with a 0.2 s exposure time.

The colony-measurer Python program (https://github.com/gwmarrah/colony-measurer; Marrah, 2021) was employed to quantify the size of bacterial colonies by pixel measurement. Images were prepared for size quantification by cropping each lane of a drip plate as an individual 8-bit image. ImageJ (Schneider et al., 2012) and colSizeMeasurer.py were used to determine the background pixel intensity and minimum/maximum colony sizes to be measured, respectively. These values were used to refine the parameters in colSizeAnalyzer.py for accurate measurement.

Immunoprecipitation and western blot

P. aeruginosa strains containing plasmid-borne NrnC_{Bh}-HA were grown overnight, followed by dilution to an OD₆₀₀ = 0.1 in fresh LB supplemented with 60 μg/ml gentamicin. Cultures were allowed to grow to an OD₆₀₀ = 0.8. Arabinose was added to a final concentration of 0.2% to induce protein expression for 2 hr at 37 °C. Following induction, cultures were normalized by OD, pelleted, and flash frozen in liquid nitrogen. Cells were resuspended in lysis buffer (150 mM NaCl, 25 mM Tris-Cl pH 7.5) followed by sonication. Anti-HA resin (Sigma) was prewashed with lysis buffer. Resin was added to the cleared lysate and incubated with rotation for 1 hr at 4 °C. Following binding, the HA resin was washed with lysis buffer, boiled in SDS loading buffer, and resolved by SDS-PAGE. Western blot transfer to a PVDF membrane proceeded for 90 min at constant 0.25 A, followed by overnight blocking with superblock (ThermoFisher) at 4 °C. Rabbit anti-HA primary antibody (Takara Bio) was diluted to 1:100 in TBS-T and incubated with the membrane for 1 hr at 20 °C. Following washes with TBS-T, an HRP-conjugated, anti-rabbit antibody (GE Life Sciences) was diluted to 1:5000 in TBS-T and incubated with the membrane for 30 min at 20 °C. The membrane was washed with TBS-T before treating with SuperSignal West Femto (ThermoFisher) ECL reagent, followed by imaging with a Bio-Rad Chemidoc system.

Size-exclusion chromatography-coupled multiangle light scattering (SEC-MALS)

Purified, wild-type or mutant variant $NrnC_{Bh}$ at 2 mg/ml (85 μ M) was injected onto a Superdex 200 Increase 10/300 gel filtration column (GE Healthcare) equilibrated with gel filtration buffer (25 mM Tris-Cl, pH 7.5, 150 mM NaCl). Size-exclusion chromatography was coupled to an in-line, static 18-angle light scattering detector (DAWN HELEOS-II, Wyatt Technology) and a refractive index detector (Optilab T-rEX, Wyatt Technology). Data were collected every second. Data analysis was performed with Astra 6.1 (Wyatt Technology) yielding the molar mass and mass distribution (polydispersity) of the sample. Monomeric BSA (Sigma; 5 mg/ml) was used as a control sample and to normalize the light scattering detectors.

Measuring dissociation constant (K_d) and binding specificity by DraCALA

To measure K_{cl} , the purified protein was serially diluted in binding buffer (10 mM Tris-HCl, pH 8, 100 mM NaCl, and 5 mM CaCl₂). Each dilution was mixed with ³²P-lableled substrate and spotted onto nitrocellulose. The dried nitrocellulose was exposed to a phosphorimager screens, scanned, and analyzed as previously described (*Roelofs et al., 2011*). The fraction bound was plotted against protein concentration using the program Prism. For competition experiments to determine binding specificity, 100 μ M of unlabeled nucleotides were mixed with ³²P-labeled pGG; the mixtures were added 200 nM of purified NrnC.



Biochemical assay of RNase activity

The reactions were performed by adding the indicated concentration of enzyme to the indicated concentration of substrate containing a tracer, consisting of 5'-end ³²P-labeled substrate with the same length and sequence, in reaction buffer (10 mM Tris-HCl, pH 8, 100 mM NaCl, and 5 mM MgCl₂). Reactions are stopped at indicated time points by the addition of 0.2 M EDTA. The samples were mixed with loading buffer (4 M urea, 20% sucrose, 0.1% SDS, 0.05% bromophenol blue, 0.05% xylene cyanole FF, and 1× TBE), and separated by electrophoresis on 20% polyacrylamide gels.

DNase activity measurement

DNase activity was assessed using an unspecific 1.5 kb PCR fragment, either with blunt ends or after restriction digestion with either Kpnl, Ndel, or Notl (New England Biolabs). CIP (New England Biolabs) was used to dephosphorylate overhangs, and PNK (New England Biolabs) was used to phosphorylate blunt PCR products. NaCl, MgCl₂, and MnCl₂ were added to the concentration indicated in the figures, with concentrations of NrnC and DNA at 1 μ M and 20 nM, respectively, except where indicated otherwise in the figure. Reactions were incubated for 30 min or the indicated time at 37 °C. Reactions were stopped by the addition of a stop buffer containing proteinase K (Qiagen) and EDTA (JT Baker) to a final concentration of 0.1 mAU proteinase K and 10 mM EDTA, followed by incubation at 50 °C for 30 min. Samples were resolved by electrophoresis in a 1% agarose gel containing GelRed stain (Biotium) and imaged by UV visualization in a GelDocXR system (Bio-Rad).

Degradation of oligonucleotides by NrnC

5'-Hydroxyl DNA and RNA oligonucleotides were purchased from Integrated DNA Technologies (IDT). Indicated DNA and RNA oligonucleotides were 5'end-radiolabeled with 32 P γ -ATP using T4 Polynucleotide Kinase. The radiolabeled DNA or RNA oligonucleotides were annealed with the complementary DNA or RNA, respectively, by heating at 95 °C for 10 min in a heat block followed by removal of the heat block from the heat source and slow cooling to room temperature. NrnC (5 nM) was added to 32 P-labeled substrates (3.3 nM) in reaction buffer. Reactions were stopped at indicated times. Short RNA or DNA oligos were analyzed by polyethyleneimine-cellulose TLC plates. The TLC plates were developed by saturated NH $_4$ SO $_4$ and 1.5 M KH $_2$ PO $_4$. For longer annealed DNA or RNA oligonucleotides, the reactions were separated by 20% urea PAGE, imaged using a Fujifilm FLA-7000 phosphorimager.

Identification of RNase homologs

For each group of RNases, a list of seed protein sequences was manually prepared with Uniprot entry names: Orn (ORN_PSEAE, ORN_ECOLI, ORN_HUMAN, ORN_STRGR, ORN_CORDI, ORN_BURMA, ORN_YEAST, ORN_VIBCH), NrnA (NRNA_BACSU, NRNA_MYCPN, NRNA_THET8, NRNA_MYCTU, A0A3R9HUU0_STRSA), NrnB (NRNB_BACSU, A0A5C5X7X8_9BACT), NrnC (A9CG28_AGRFC, G4VUY7_9RHIZ, A1UU18_BARBK), RNase T (RNT_ECOLI, RNT_VIBCH, RNT_BUCAP, RNT_HAEIN, RNT_XYLFA), and RNase D (RND_ECOLI, Q9ZD81_RICPR, RND_HAEIN, I6XF17_MYCTU).

Initially a seed alignment was prepared for each RNase family using T-COFFEE (Notredame et al., 2000) in the Expresso structural alignment mode (Armougom et al., 2006). A search on the 2020_03 release of UniprotKB was performed with an HMM prepared from these alignments with hmmsearch from HMMER 3.3 (Eddy, 2011). Results were filtered by two criteria, a hit score above 125 and a template/query length ratio between 0.8 and 1.2. Search hits were used to construct a new multiple sequence alignment with MAFFT in E-INS-i mode (Katoh et al., 2005). The hmmsearch was repeated with an HMM constructed from this expanded alignment and results were filtered with the same hit score cutoff but a more generous template/query length ratio between 0.6 and 1.5. The resulting hits were considered to be the final list for each RNase family, with any sequences found in multiple categories assigned to the category for which it had a higher hit score.

To determine whether a particular taxa contained homologs for each RNase group, the total number of proteins for each taxon in the NCBI taxon database present in our dataset was counted (**Federhen**, **2012**). The average number of proteins per genome for each taxon was determined for all genomes annotated as a descendent taxon available in the NCBI genome database. Finally, the number of homologs found in each taxonomic category was calculated as a fraction of the total proteins in that taxon, multiplied by the average genome size to get an average presence-per-genome. For



visualization purposes, values above 0.5 are considered present and non-zero values below 0.5 are potentially or partially present. The minimal species tree was extracted from the NCBI taxonomy database using ETE3 (*Huerta-Cepas et al., 2016*), followed by visualization of the resulting tree and annotation with iTOL (*Letunic and Bork, 2019*).

All commands and code from this analysis were constructed as a reproducible SnakeMake pipeline (*Köster and Rahmann, 2018*) available at https://github.com/jgoodson/rnases, (copy archived at swh:1:rev:66b266487bfafb3dfc8917dbfd710c9ef7dc0220;*Goodson, 2021 Goodson, 2021*) (commit 66b2664 used in current versions of the figures).

Phylogenetics of DnaQ-family RNases

To construct a phylogenetic tree of the DnaQ-fold RNases, the final sequences identified from the previous analysis for each family were clustered by sequence identity with MMSeqs2 (Steinegger and Söding, 2017). Targeting a final sequence count of 600, the sequence identity threshold was determined for each family necessary to approximately maintain the original proportion of each family in the final representatives (30% for Orn, 45% for NrnC, 50% for RNase T, and 30% for RNase D). From these cluster representatives, a multiple sequence alignment was constructed using MAFFT in E-INS-i mode using DASH to obtain additional structural homologs (Rozewicki et al., 2019). The alignment was trimmed by removing the additional DASH sequences and columns with more than 90% gaps. The most appropriate evolutionary model was determined with IQ-TREE ModelFinder (LG + R8) and a phylogenetic tree was constructed using IQ-TREE 2.1.1 with 10,000 UFBoot replicates, and some modified parameters for expanded tree search (additional UFBoot NNI search, initial SPR search radius 20, 500 initial trees, initial search on 100 best trees, maintenance of the 50 best trees, and 500 iterations without improvement as stopping criteria) (Hoang et al., 2018; Kalyaanamoorthy et al., 2017; Minh et al., 2020). The tree was rooted with midpoint rooting on the long internal branch between RNaseT/Orn and RNaseD/NrnC. Sequence logos were created from monophyletic subgroup alignments using Logomaker (Tareen and Kinney, 2020).

Data deposition

The atomic coordinates and structure factors have been deposited in the Protein Data Bank, https://www.rcsb.org/ (PDB ID codes 7MPL, 7MPM, 7MPN, 7MPO, 7MPP, 7MPQ, 7MPR, 7MPS, 7MPT, 7MPU, 7MQB/EMD-23941, 7MQD/EMD-23943, 7MQF/EMD-23945, 7MQH/EMD-23947, 7MQC/EMD-23942, 7MQE/EMD-23944, 7MQG/EMD-23946, 7MQI/EMD-23948).

Acknowledgements

This work is based upon research conducted at the Northeastern Collaborative Access Team beamlines, which are funded by the National Institute of General Medical Sciences from the National Institutes of Health (P30 GM124165). The Eiger 16 M detector on 24-ID-E is funded by a NIH-ORIP HEI grant (S10OD021527). This research used resources of the Advanced Photon Source, a US Department of Energy (DOE) Office of Science User Facility operated for the DOE Office of Science by Argonne National Laboratory under Contract No. DE-AC02-06CH11357. Additional crystallographic research was conducted at the Center for High Energy X-ray Sciences (CHEXS), Cornell High Energy Synchrotron Source (CHESS), which is supported by the NSF under award DMR-1829070. The MacCHESS resource is supported by NIGMS award 1-P30-GM124166-01A1 and NYSTAR. This work made use of the Cornell Center for Materials Research Shared Facilities, which are supported through the NSF MRSEC program (DMR-1719875). The funding sources were not involved in study design, data collection and interpretation, or the decision to submit the work for publication.



Additional information

Funding

Funder	Grant reference number	Author
National Institutes of Health	R01AI142400	Vincent T Lee
National Institutes of Health	R01GM123609	Holger Sondermann
National Institutes of Health	R35GM136258	J Christopher Fromme

The funders had no role in study design, data collection and interpretation, or the decision to submit the work for publication.

Author contributions

Justin D Lormand, Conceptualization, Data curation, Formal analysis, Investigation, Validation, Visualization, Writing - original draft, Writing - review and editing; Soo-Kyoung Kim, Conceptualization, Data curation, Formal analysis, Investigation, Validation, Writing - review and editing; George A Walters-Marrah, Formal analysis, Investigation, Software, Validation, Writing - review and editing; Bryce A Brownfield, Data curation, Formal analysis, Investigation, Validation, Visualization, Writing - review and editing; J Christopher Fromme, Data curation, Formal analysis, Validation, Writing - review and editing; Wade C Winkler, Conceptualization, Funding acquisition, Validation, Writing - review and editing; Jonathan R Goodson, Conceptualization, Data curation, Formal analysis, Investigation, Software, Validation, Visualization, Writing - original draft, Writing - review and editing; Vincent T Lee, Holger Sondermann, Conceptualization, Data curation, Formal analysis, Funding acquisition, Investigation, Project administration, Supervision, Validation, Visualization, Writing - original draft, Writing - review and editing

Author ORCIDs

Justin D Lormand http://orcid.org/0000-0002-7803-4716

J Christopher Fromme http://orcid.org/0000-0002-8837-0473

Vincent T Lee http://orcid.org/0000-0002-3593-0318

Holger Sondermann http://orcid.org/0000-0003-2211-6234

Decision letter and Author response

Decision letter https://doi.org/10.7554/eLife.70146.sa1 Author response https://doi.org/10.7554/eLife.70146.sa2

Additional files

Supplementary files

- Supplementary file 1. X-ray data collection and refinement statistics.
- Supplementary file 2. Cryo-electron microscopy model validation statistics.
- Transparent reporting form

Data availability

The atomic coordinates and structure factors have been deposited in the Protein Data Bank, https://www.rcsb.org/ (PDB ID codes 7MPL, 7MPM, 7MPN, 7MPO, 7MPP, 7MPQ, 7MPR, 7MPS, 7MPT, 7MPU, 7MQB/EMD-23941, 7MQD/EMD-23943, 7MQF/EMD-23945, 7MQH/EMD-23947, 7MQC/EMD-23942, 7MQE/EMD-23944, 7MQG/EMD-23946, 7MQI/EMD-23948).

The following dataset was generated:

Author(s)	Year	Dataset title	Dataset URL	Database and Identifier
Lormand JD,	2021	Bartonella henselae NrnC	https://www.rcsb.org/	RCSB Protein Data Bank,
Sondermann H		bound to pGG	structure/7MPL	7MPL



Author(s)	Year	Dataset title	Dataset URL	Database and Identifier
Lormand JD, Sondermann H	2021	Bartonella henselae NrnC bound to pAA	https://www.rcsb.org/ structure/7MPM	RCSB Protein Data Bank, 7MPM
Lormand JD, Sondermann H	2021	Bartonella henselae NrnC bound to pGC	https://www.rcsb.org/ structure/7MPN	RCSB Protein Data Bank, 7MPN
Lormand JD, Sondermann H	2021	Bartonella henselae NrnC bound to pAp	https://www.rcsb.org/ structure/7MPO	RCSB Protein Data Bank, 7MPO
Lormand JD, Sondermann H	2021	Bartonella henselae NrnC cleaving pGG in the presence of Mg2+	https://www.rcsb.org/ structure/7MPP	RCSB Protein Data Bank, 7MPP
Lormand JD, Sondermann H	2021	Bartonella henselae NrnC cleaving pGG in the presence of Mn2+	https://www.rcsb.org/ structure/7MPQ	RCSB Protein Data Bank, 7MPQ
Lormand JD, Sondermann H	2021	Brucella melitensis NrnC	https://www.rcsb.org/ structure/7MPR	RCSB Protein Data Bank, 7MPR
Lormand JD, Sondermann H	2021	Brucella melitensis NrnC with engaged loop	https://www.rcsb.org/ structure/7MPS	RCSB Protein Data Bank, 7MPS
Lormand JD, Sondermann H	2021	Brucella melitensis NrnC with bound Mg2+	https://www.rcsb.org/ structure/7MPT	RCSB Protein Data Bank, 7MPT
Lormand JD, Sondermann H	2021	Brucella melitensis NrnC bound to pGG	https://www.rcsb.org/ structure/7MPU	RCSB Protein Data Bank, 7MPU
Lormand JD, Brownfield B, Fromme JC, Sondermann H	2021	Bartonella henselae NrnC bound to pGG. D4 Symmetry	https://www.rcsb.org/ structure/7MQB	RCSB Protein Data Bank, 7MQB/EMD-23941
Lormand JD, Brownfield B, Fromme JC, Sondermann H	2021	Bartonella henselae NrnC complexed with pAGG. D4 symmetry	https://www.rcsb.org/ structure/7MQD	RCSB Protein Data Bank, 7MQD/EMD-23943
Lormand JD, Brownfield B, Fromme JC, Sondermann H	2021	Bartonella henselae NrnC complexed with pAAAGG. D4 symmetry	https://www.rcsb.org/ structure/7MQF	RCSB Protein Data Bank, 7MQF/EMD-23945
Lormand JD, Brownfield B, Fromme JC, Sondermann H	2021	Bartonella henselae NrnC complexed with pAAAGG in the presence of Ca2+. D4 Symmetry	https://www.rcsb.org/ structure/7MQH	RCSB Protein Data Bank, 7MQH/EMD-23947
Lormand JD, Brownfield B, Fromme JC, Sondermann H	2021	Bartonella henselae NrnC bound to pGG. C1 reconstruction	https://www.rcsb.org/ structure/7MQC	RCSB Protein Data Bank, 7MQC/EMD-23942
Lormand JD, Brownfield B, Fromme JC, Sondermann H	2021	Bartonella henselae NrnC complexed with pAGG. C1 reconstruction	https://www.rcsb.org/ structure/7MQE	RCSB Protein Data Bank, 7MQE/EMD-23944
Lormand JD, Brownfield B, Fromme JC, Sondermann H	2021	Bartonella henselae NrnC complexed with pAAAGG. C1 reconstruction	https://www.rcsb.org/ structure/7MQG	RCSB Protein Data Bank, 7MQG/EMD-23946
Lormand JD, Brownfield B, Fromme JC, Sondermann H	2021	Bartonella henselae NrnC complexed with pAAAGG in the presence of Ca2+. C1 reconstruction	https://www.rcsb.org/ structure/7MQI	RCSB Protein Data Bank, 7MQI/EMD-23948

References

Adams PD, Afonine PV, Bunkóczi G, Chen VB, Davis IW, Echols N, Headd JJ, Hung L-W, Kapral GJ, Grosse-Kunstleve RW, McCoy AJ, Moriarty NW, Oeffner R, Read RJ, Richardson DC, Richardson JS,



- Terwilliger TC, Zwart PH. 2010. PHENIX: A comprehensive python-based system for macromolecular structure solution. *Acta Crystallographica*. *Section D, Biological Crystallography* **66**: 213–221. DOI: https://doi.org/10.1107/s0907444909052925, PMID: 20124702
- **Afonine PV**, Poon BK, Read RJ, Sobolev OV, Terwilliger TC, Urzhumtsev A, Adams PD. 2018. Real-space refinement in PHENIX for cryo-em and crystallography. *Acta Crystallographica*. *Section D, Structural Biology* **74**: 531–544. DOI: https://doi.org/10.1107/s2059798318006551, PMID: 29872004
- Armougom F, Moretti S, Poirot O, Audic S, Dumas P, Schaeli B, Keduas V, Notredame C. 2006. Expresso: Automatic incorporation of structural information in multiple sequence alignments using 3d-coffee. *Nucleic Acids Research* 34: 604-608. DOI: https://doi.org/10.1093/nar/gkl092, PMID: 16845081
- Chin KH, Yang CY, Chou CC, Wang AH, Chou SH. 2006. The crystal structure of XC847 from Xanthomonas campestris: a 3'-5' oligoribonuclease of DnaQ fold family with a novel opposingly shifted helix. *Proteins* 65: 1036–1040. DOI: https://doi.org/10.1002/prot.21148
- Choi KH, Kumar A, Schweizer HP. 2006. A 10-min method for preparation of highly electrocompetent Pseudomonas aeruginosa cells: application for DNA fragment transfer between chromosomes and plasmid transformation. Journal of Microbiological Methods 64: 391–397. DOI: https://doi.org/10.1016/j.mimet.2005.06.001
- Christen B, Abeliuk E, Collier JM, Kalogeraki VS, Passarelli B, Coller JA, Fero MJ, McAdams HH, Shapiro L. 2011.
 The essential genome of a bacterium. *Molecular Systems Biology* 7: 528. DOI: https://doi.org/10.1038/msb. 2011.58
- Chu LY, Agrawal S, Chen YP, Yang WZ, Yuan HS. 2019. Structural insights into nanoRNA degradation by human Rexo2. RNA 25: 737–746. DOI: https://doi.org/10.1261/rna.070557.119, PMID: 30926754
- Cohen D, Mechold U, Nevenzal H, Yarmiyhu Y, Randall TE, Bay DC, Rich JD, Parsek MR, Kaever V, Harrison JJ, Banin E. 2015. Oligoribonuclease is a central feature of cyclic diguanylate signaling in *Pseudomonas aeruginosa*. PNAS 112: 11359–11364. DOI: https://doi.org/10.1073/pnas.1421450112
- **Datta AK**, Niyogi K. 1975. A novel oligoribonuclease of *Escherichia coli* II. Mechanism of Action. *J Biol Chem* **250**: 7313–7319.
- Dehio C. 2005. Bartonella-host-cell interactions and vascular tumour formation. *Nature Reviews. Microbiology* 3: 621–631. DOI: https://doi.org/10.1038/nrmicro1209
- **Druzhinin SY**, Tran NT, Skalenko KS, Goldman SR, Knoblauch JG, Dove SL, Nickels BE. 2015. A Conserved Pattern of Primer-Dependent Transcription Initiation in *Escherichia coli* and *Vibrio cholerae* Revealed by 5' RNA-seq. *PLOS Genetics* 11: e1005348. DOI: https://doi.org/10.1371/journal.pgen.1005348
- Eddy SR. 2011. Accelerated Profile HMM Searches. *PLOS Computational Biology* 7: e1002195. DOI: https://doi.org/10.1371/journal.pcbi.1002195
- Edgar RC. 2004. MUSCLE: multiple sequence alignment with high accuracy and high throughput. *Nucleic Acids Research* 32: 1792–1797. DOI: https://doi.org/10.1093/nar/gkh340
- Emsley P, Lohkamp B, Scott WG, Cowtan K. 2010. Features and development of Coot. Acta Crystallographica. Section D, Biological Crystallography 66: 486–501. DOI: https://doi.org/10.1107/s0907444910007493
- Evans P. 2006. Scaling and assessment of data quality. Acta Crystallographica. Section D, Biological Crystallography 62: 72–82. DOI: https://doi.org/10.1107/s0907444905036693
- Fang M, Zeisberg WM, Condon C, Ogryzko V, Danchin A, Mechold U. 2009. Degradation of nanoRNA is performed by multiple redundant RNases in *Bacillus subtilis*. *Nucleic Acids Research* 37: 5114–5125. DOI: https://doi.org/10.1093/nar/gkp527
- Federhen S. 2012. The NCBI Taxonomy database. *Nucleic Acids Research* 40: D136–D143. DOI: https://doi.org/10.1093/nar/gkr1178
- Galperin MY, Koonin E. 2012. Divergence and convergence in enzyme evolution. The Journal of Biological Chemistry 287: 21–28. DOI: https://doi.org/10.1074/jbc.R111.241976
- **Ghosh 5**, Deutscher MP. 1999. Oligoribonuclease is an essential component of the mRNA decay pathway. *PNAS* **96**: 4372–4377. DOI: https://doi.org/10.1073/pnas.96.8.4372
- Goldman SR, Sharp JS, Vvedenskaya IO, Livny J, Dove SL, Nickels BE. 2011. NanoRNAs prime transcription initiation in vivo. *Molecular Cell* 42: 817–825. DOI: https://doi.org/10.1016/j.molcel.2011.06.005
- Goodson J. 2021. Rnases. swh:1:rev:66b266487bfafb3dfc8917dbfd710c9ef7dc0220. Software Heritage. https://archive.softwareheritage.org/swh:1:dir:948afe1bbb90435abda675896f596c93577ee420;origin=https://github.com/jgoodson/rnases;visit=swh:1:snp:26ecae94f2928de36d0bdac09fe4eb492c208138;anchor=swh:1:rev:66b266487bfafb3dfc8917dbfd710c9ef7dc0220
- **Greenfield RA**, Drevets DA, Machado LJ, Voskuhl GW, Cornea P, Bronze MS. 2002. Bacterial pathogens as biological weapons and agents of bioterrorism. *The American Journal of the Medical Sciences* **323**: 299–315. DOI: https://doi.org/10.1097/00000441-200206000-00003
- Hmelo LR, Borlee BR, Almblad H, Love ME, Randall TE, Tseng BS, Lin C, Irie Y, Storek KM, Yang JJ, Siehnel RJ, Howell PL, Singh PK, Tolker-Nielsen T, Parsek MR, Schweizer HP, Harrison JJ. 2015. Precision-engineering the *Pseudomonas aeruginosa* genome with two-step allelic exchange. *Nature Protocols* 10: 1820–1841. DOI: https://doi.org/10.1038/nprot.2015.115
- Hoang DT, Chernomor O, von Haeseler A, Minh BQ, Vinh LS. 2018. UFBoot2: Improving the Ultrafast Bootstrap Approximation. *Molecular Biology and Evolution* 35: 518–522. DOI: https://doi.org/10.1093/molbev/msx281
- Huerta-Cepas J, Serra F, Bork P. 2016. ETE 3: reconstruction, analysis, and visualization of phylogenomic data. Molecular Biology and Evolution 33: 1635–1638. DOI: https://doi.org/10.1093/molbev/msw046



- Huerta-Cepas J, Szklarczyk D, Heller D, Hernández-Plaza A, Forslund SK, Cook H, Mende DR, Letunic I, Rattei T, Jensen LJ, von Mering C, Bork P. 2019. eggNOG 5.0: a hierarchical, functionally and phylogenetically annotated orthology resource based on 5090 organisms and 2502 viruses. Nucleic Acids Research 47: D309–D314. DOI: https://doi.org/10.1093/nar/gky1085
- Kabsch W. 2010. Integration, scaling, space-group assignment and post-refinement. Acta Crystallographica. Section D, Biological Crystallography 66: 133–144. DOI: https://doi.org/10.1107/s0907444909047374
- Kalyaanamoorthy S, Minh BQ, Wong TKF, von Haeseler A, Jermiin LS. 2017. ModelFinder: fast model selection for accurate phylogenetic estimates. *Nature Methods* 14: 587–589. DOI: https://doi.org/10.1038/nmeth.4285
- Kamp HD, Patimalla-Dipali B, Lazinski DW, Wallace-Gadsden F, Camilli A. 2013. Gene fitness landscapes of *Vibrio cholerae* at important stages of its life cycle. *PLOS Pathogens* 9: e1003800. DOI: https://doi.org/10.1371/journal.ppat.1003800
- Katoh K, Kuma K, Toh H, Miyata T. 2005. MAFFT version 5: improvement in accuracy of multiple sequence alignment. *Nucleic Acids Research* 33: 511–518. DOI: https://doi.org/10.1093/nar/gki198
- Keegan RM, McNicholas SJ, Thomas JMH, Simpkin AJ, Simkovic F, Uski V, Ballard CC, Winn MD, Wilson KS, Rigden DJ. 2018. Recent developments in MrBUMP: better search-model preparation, graphical interaction with search models, and solution improvement and assessment. Acta Crystallographica. Section D, Structural Biology 74: 167–182. DOI: https://doi.org/10.1107/s2059798318003455
- Kim SK, Lormand JD, Weiss CA, Eger KA, Turdiev H, Turdiev A, Winkler WC, Sondermann H, Lee VT. 2019. A dedicated diribonuclease resolves a key bottleneck for the terminal step of RNA degradation. *eLife* 8:e46313. DOI: https://doi.org/10.7554/eLife.46313
- Köster J, Rahmann S. 2018. Snakemake-a scalable bioinformatics workflow engine. *Bioinformatics* **34**: 3600. DOI: https://doi.org/10.1093/bioinformatics/bty350
- Krissinel E, Henrick K. 2007. Inference of macromolecular assemblies from crystalline state. *Journal of Molecular Biology* 372: 774–797. DOI: https://doi.org/10.1016/j.jmb.2007.05.022
- Letunic I, Bork P. 2019. Interactive Tree of Life (iTOL) v4: Recent updates and new developments. *Nucleic Acids Research* 47: W256–W259. DOI: https://doi.org/10.1093/nar/gkz239, PMID: 30931475
- Liao H, Liu M, Guo X. 2018. The special existences: nanoRNA and nanoRNase. *Microbiological Research* 207: 134–139. DOI: https://doi.org/10.1016/j.micres.2017.11.014
- Liebschner D, Afonine P, Baker ML, Bunkóczi G, Chen VB, Croll T, Hintze B, Hung LW, Jain S, McCoy AJ, Moriarty NW, Oeffner RD, Poon BK, Prisant MG, Read RJ, Richardson JS, Richardson DC, Sammito MD, Sobolev O, Stockwell DH, et al. 2019. Macromolecular structure determination using X-rays, neutrons and electrons: recent developments in Phenix. Acta Crystallographica. Section D, Structural Biology 75: 861–877. DOI: https://doi.org/10.1107/s2059798319011471
- Liu MF, Cescau S, Mechold U, Wang J, Cohen D, Danchin A, Boulouis HJ, Biville F. 2012. Identification of a novel nanoRNase in Bartonella. *Microbiology* **158**: 886–895. DOI: https://doi.org/10.1099/mic.0.054619-0
- Marrah GW. 2021. Colony-measurer. 3799802. Github. https://github.com/gwmarrah/colony-measurer
- Mechold U, Ogryzko V, Ngo S, Danchin A. 2006. Oligoribonuclease is a common downstream target of lithium-induced pAp accumulation in *Escherichia coli* and human cells. *Nucleic Acids Research* 34: 2364–2373. DOI: https://doi.org/10.1093/nar/gkl247, PMID: 16682444
- Mechold U, Fang G, Ngo S, Ogryzko V, Danchin A. 2007. Ytql from *Bacillus subtilis* has both oligoribonuclease and pAp-phosphatase activity. *Nucleic Acids Research* **35**: 4552–4561. DOI: https://doi.org/10.1093/nar/gkm462
- Minh BQ, Schmidt HA, Chernomor O, Schrempf D, Woodhams MD, von Haeseler A, Lanfear R. 2020. IQ-TREE 2: New Models and Efficient Methods for Phylogenetic Inference in the Genomic Era. *Molecular Biology and Evolution* 37: 1530–1534. DOI: https://doi.org/10.1093/molbev/msaa015
- Morin A, Eisenbraun B, Key J, Sanschagrin PC, Timony MA, Ottaviano M, Sliz P. 2013. Collaboration gets the most out of software. *eLife* 2: e01456. DOI: https://doi.org/10.7554/eLife.01456
- Newman JR, Fuqua C. 1999. Broad-host-range expression vectors that carry the L-arabinose-inducible Escherichia coli araBAD promoter and the araC regulator. Gene 227: 197–203. DOI: https://doi.org/10.1016/s0378-1119(98)00601-5
- Nguyen LH, Erzberger JP, Root J, Wilson DM. 2000. The human homolog of *Escherichia coli* Orn degrades small single-stranded RNA and DNA oligomers. *The Journal of Biological Chemistry* 275: 25900–25906. DOI: https://doi.org/10.1074/jbc.M002672200
- Nicholls TJ, Spåhr H, Jiang S, Siira SJ, Koolmeister C, Sharma S, Kauppila JHK, Jiang M, Kaever V, Rackham O, Chabes A, Falkenberg M, Filipovska A, Larsson NG, Gustafsson CM. 2019. Dinucleotide Degradation by REXO2 Maintains Promoter Specificity in Mammalian Mitochondria. *Molecular Cell* 76: 784–796. DOI: https://doi.org/10.1016/j.molcel.2019.09.010
- Niyogi SK, Datta AK. 1975. A novel oligoribonuclease of Escherichia coli. I. Isolation and properties. The Journal of Biological Chemistry 250: 7307–7312 PMID: 240824.,
- Notredame C, Higgins DG, Heringa J. 2000. T-Coffee: A novel method for fast and accurate multiple sequence alignment. *Journal of Molecular Biology* 302: 205–217. DOI: https://doi.org/10.1006/jmbi.2000.4042
- Omelchenko M, Galperin MY, Wolf Y, Koonin E. 2010. Non-homologous isofunctional enzymes: a systematic analysis of alternative solutions in enzyme evolution. *Biology Direct* 5: 31. DOI: https://doi.org/10.1186/1745-6150-5-31



- Orr MW, Donaldson GP, Severin GB, Wang J, Sintim HO, Waters CM, Lee VT. 2015. Oligoribonuclease is the primary degradative enzyme for pGpG in *Pseudomonas aeruginosa* that is required for cyclic-di-GMP turnover. *PNAS* 112: E5048–E5057. DOI: https://doi.org/10.1073/pnas.1507245112
- Orr MW, Weiss CA, Severin GB, Turdiev H, Kim SK, Turdiev A, Liu K, Tu BP, Waters CM, Winkler WC, Lee VT. 2018. A Subset of Exoribonucleases Serve as Degradative Enzymes for pGpG in c-di-GMP Signaling. *Journal of Bacteriology* 200: 00300–00318. DOI: https://doi.org/10.1128/jb.00300-18
- Palace SG, Proulx MK, Lu S, Baker RE, Goguen JD. 2014. Genome-wide mutant fitness profiling identifies nutritional requirements for optimal growth of Yersinia pestis in deep tissue. MBio 5: 01385-14. DOI: https://doi.org/10.1128/mBio.01385-14
- Pappas G, Papadimitriou P, Akritidis N, Christou L, Tsianos E. 2006. The new global map of human brucellosis. The Lancet. Infectious Diseases 6: 91–99. DOI: https://doi.org/10.1016/s1473-3099(06)70382-6
- Park J, Lee SY, Jeong H, Kang MG, Van Haute L, Minczuk M, Seo JK, Jun Y, Myung K, Rhee HW, Lee C. 2019. The structure of human EXD2 reveals a chimeric 3' to 5' exonuclease domain that discriminates substrates via metal coordination. *Nucleic Acids Research* 47: 7078–7093. DOI: https://doi.org/10.1093/nar/gkz454
- Pettersen EF, Goddard TD, Huang CC, Meng EC, Couch GS, Croll T, Morris JH, Ferrin TE. 2021. UCSF ChimeraX: Structure visualization for researchers, educators, and developers. *Protein Science* 30: 70–82. DOI: https://doi.org/10.1002/pro.3943
- Punjani A, Rubinstein JL, Fleet DJ, Brubaker MA. 2017. cryoSPARC: algorithms for rapid unsupervised cryo-EM structure determination. *Nature Methods* 14: 290–296. DOI: https://doi.org/10.1038/nmeth.4169
- Rahme LG, Stevens EJ, Wolfort SF, Shao J, Tompkins RG, Ausubel FM. 1995. Common virulence factors for bacterial pathogenicity in plants and animals. *Science* 268: 1899–1902. DOI: https://doi.org/10.1126/science. 7604262
- Roelofs KG, Wang J, Sintim HO, Lee VT. 2011. Differential radial capillary action of ligand assay for high-throughput detection of protein-metabolite interactions. PNAS 108: 15528–15533. DOI: https://doi.org/10.1073/pnas.1018949108
- Rosta E, Yang W, Hummer G. 2014. Calcium inhibition of ribonuclease H1 two-metal ion catalysis. *Journal of the American Chemical Society* 136: 3137–3144. DOI: https://doi.org/10.1021/ja411408x
- Rozewicki J, Li S, Amada KM, Standley DM, Katoh K. 2019. MAFFT-DASH: integrated protein sequence and structural alignment. *Nucleic Acids Research* 47: W5–W10. DOI: https://doi.org/10.1093/nar/gkz342
- Schmier BJ, Nelersa CM, Malhotra A. 2017. Structural Basis for the Bidirectional Activity of Bacillus nanoRNase NrnA. Scientific Reports 7: 11085. DOI: https://doi.org/10.1038/s41598-017-09403-x
- Schneider CA, Rasband WS, Eliceiri KW. 2012. NIH Image to ImageJ: 25 years of image analysis. Nature Methods 9: 671–675. DOI: https://doi.org/10.1038/nmeth.2089
- Steinegger M, Söding J. 2017. MMseqs2 enables sensitive protein sequence searching for the analysis of massive data sets. *Nature Biotechnology* **35**: 1026–1028. DOI: https://doi.org/10.1038/nbt.3988
- Sternon JF, Godessart P, Gonçalves de Freitas R, Van der Henst M, Poncin K, Francis N, Willemart K, Christen M, Christen B, Letesson JJ, Bolle D. 2018. Transposon Sequencing of Brucella abortus Uncovers Essential Genes for Growth In Vitro and Inside Macrophages. *Infection and Immunity* 86: 00312–00318. DOI: https://doi.org/10.1128/iai.00312-18
- Tareen A, Kinney JB. 2020. Logomaker: beautiful sequence logos in Python. *Bioinformatics* 36: 2272–2274. DOI: https://doi.org/10.1093/bioinformatics/btz921
- Vvedenskaya IO, Sharp JS, Goldman SR, Kanabar PN, Livny J, Dove SL, Nickels BE. 2012. Growth phase-dependent control of transcription start site selection and gene expression by nanoRNAs. Genes & Development 26: 1498–1507. DOI: https://doi.org/10.1101/gad.192732.112
- Wasmuth E, Januszyk K, Lima CD. 2014. Structure of an Rrp6-RNA exosome complex bound to poly(A) RNA. Nature 511: 435–439. DOI: https://doi.org/10.1038/nature13406
- Winn MD, Ballard CC, Cowtan KD, Dodson EJ, Emsley P, Evans PR, Keegan RM, Krissinel EB, Leslie AG, McCoy A, McNicholas SJ, Murshudov GN, Pannu NS, Potterton EA, Powell HR, Read RJ, Vagin A, Wilson KS. 2011. Overview of the CCP4 suite and current developments. *Acta Crystallographica*. Section D, Biological Crystallography 67: 235–242. DOI: https://doi.org/10.1107/s0907444910045749
- Yu D, Deutscher MP. 1995. Oligoribonuclease is distinct from the other known exoribonucleases of Escherichia coli. Journal of Bacteriology 177: 4137–4139. DOI: https://doi.org/10.1128/jb.177.14.4137-4139.1995
- Yuan Z, Gao F, Yin K, Gu L. 2018. NrnC, an RNase D-Like Protein From Agrobacterium, Is a Novel Octameric Nuclease That Specifically Degrades dsDNA but Leaves dsRNA Intact. Frontiers in Microbiology 9: 3230. DOI: https://doi.org/10.3389/fmicb.2018.03230
- Zhang X, Zhu L, Deutscher MP. 1998. Oligoribonuclease is encoded by a highly conserved gene in the 3'-5' exonuclease superfamily. *Journal of Bacteriology* 180: 2779–2781. DOI: https://doi.org/10.1128/jb.180.10. 2779-2781.1998
- Zhang K. 2016. Gctf: Real-time CTF determination and correction. *Journal of Structural Biology* 193: 1–12. DOI: https://doi.org/10.1016/j.jsb.2015.11.003
- Zheng SQ, Palovcak E, Armache JP, Verba KA, Cheng Y, Agard DA. 2017. MotionCor2: anisotropic correction of beam-induced motion for improved cryo-electron microscopy. *Nature Methods* 14: 331–332. DOI: https://doi.org/10.1038/nmeth.4193
- **Zivanov** J, Nakane T, Forsberg BO, Kimanius D, Hagen WJ, Lindahl E, Scheres SH. 2018. New tools for automated high-resolution cryo-EM structure determination in RELION-3. *eLife* **7**: e42166. DOI: https://doi.org/10.7554/eLife.42166





Zuo Y, Deutscher MP. 2001. Exoribonuclease superfamilies: structural analysis and phylogenetic distribution.
 Nucleic Acids Research 29: 1017–1026. DOI: https://doi.org/10.1093/nar/29.5.1017
 Zuo Y, Wang Y, Malhotra A. 2005. Crystal structure of Escherichia coli RNase D, an exoribonuclease involved in structured RNA processing. Structure 13: 973–984. DOI: https://doi.org/10.1016/j.str.2005.04.015